

Simulations of gas-liquid flow by the Eulerian-Eulerian method: a numerical study of nine cases

Yulong Li^{a,b}, Dongyue Li^{c,d,*}

^a*School of Marine Engineering and Technology, Sun Yat-Sen University, Zhuhai, China*

^b*Southern Marine Science and Engineering Guangdong Laboratory (Zhuhai), Zhuhai, China*

^c*State Key Laboratory of Advanced Metallurgy, University of Science and Technology Beijing, China.*

^d*DYFLUID Ltd, Beijing, China*

Abstract

In this work, the Eulerian-Eulerian (E-E) method was used to investigate nine classic gas-liquid systems. These test cases were selected from different industries including chemical, nuclear, bio-processing and metallurgical engineering. Although coming from different disciplines, all the test cases can be seen as multi-phase bubbly flows. They were launched by the OpenFOAM solver `reactingTwoPhaseEulerFoam`, in which the E-E method was implemented with sophisticated numerical techniques. The governing equations and discretization procedure were firstly discussed in details. The effects of the drag force, non-drag forces, bubble induced turbulence, bubble swarm on the predicted phase fraction distribution, gas holdup, liquid velocity and turbulence variables were investigated. Our results show that the combination of drag force and turbulence dispersion force should be included to all the test cases. The drag force directly determines the global gas holdup and the vertical liquid/gas velocity. For the test cases operated at high aspect ratio (e.g., pipe flows), accurate results can only be obtained by considering lift force and wall lubrication force. In certain cases, the addition of the bubble induced model improves the predictions, whereas in other cases it predicts worse results. Meanwhile, the bubble swarm correction should be used in simulations when operated at high gas phase fraction. Further, some of the shortcomings of the E-E method are identified and recommendations for future work are made based on the

*Corresponding author. Email: li.dy@dyfluid.com (D. Li)

numerical analysis.

Keywords: Gas-liquid flows, Eulerian-Eulerian method, Bubbly flow, OpenFOAM

1. Introduction

Gas-liquid flows are encountered in a variety of applications and can be simulated by different models, such as the Eulerian-Eulerian (E-E) method, the Eulerian-Lagrangian (E-L) method and the direct method which is also called multi-phase direct numerical simulation (DNS). In the E-E method [1, 2, 3, 4, 5, 6, 7, 8], each fluid phase is considered as a continuum in the computational domain under consideration which can interpenetrate with the other fluid phase. Several averaging methods (such as volume or ensemble averaging) are used to formulate basic governing equations. In the E-L approach [2, 9, 10, 11], the continuous phase is treated in an Eulerian framework whereas the motion of individual bubbles is simulated by solving the force balance equation. The trajectories of these bubbles are computed in the control volume and averaged at the computational level. In the multi-phase DNS [12, 13, 14, 15], one employs the Navier-Stokes equations directly, without further manipulation and the topology of the interface between the two-phases is determined as part of the solution. No additional modelling assumptions are introduced. DNS requires very high resolution in order to resolve a broad range of temporal and spatial scales. These scales are associated with the topology of the interface, e.g. the size of the dispersed particles, or with the fluid motion, e.g. the eddies encountered in the turbulent motion. Resolving these scales is computationally expensive both in terms of computer memory size execution time. Therefore, DNS is restricted to only low Reynolds numbers and a few bubbles/particles due to its high computational cost.

Thanks to the computational economics, many works used the E-E method to simulate gas-liquid flows. However, as a macro-scopic method, the E-E method 1) requires constitutive models (e.g., the solid-phase stress model); 2) requires models to address the momentum and energy exchange terms (e.g., the drag model); 3) loses the characteristic feature for those

scales which is much smaller than the mesh resolution. To obtain reasonable results, suitable sub-models and parameters should be adjusted. Moreover, the observed flow field is also different for the gas-liquid flows in different industries. For example, bubble columns are quite common in chemical engineering industry. The liquid flow field in the bubble column tends to form a circulation model due to the movement of the bubbles, which is commonly referred as “Gulf-stream” or “cooling tower” flow regime. In the nuclear engineering, the phase fraction of the bubbles in vertical upward pipe shows a wall peak due to the lateral movement of the small bubbles [16, 17, 18]. Without loss of the generality, it was proven that the E-E method is able to capture the typical flow field information. However, amount of work needs to be studied for the sub-models, especially for the momentum interfacial exchange models.

The drag force, as the most important momentum interfacial exchange term, plays the most important role. It determines the bubble terminal velocity and address the coupling between the disperse phase with the continuous phase. On the other hand, the lift force and wall lubrication force play an important role in the prediction of the lateral movement of the bubbles. Therefore, a correct description of the lift coefficient and wall force coefficient is crucial in order to model this transversal force correctly. The turbulence dispersion force acts as a driving force for bubbles to move from areas with higher phase fractions to areas of lower phase fraction. It arises due to the pressure variations in the continuous phase that are not resolved at meso-scale. When the gas bubbles are not diluted nor isolated, their momentum boundary layers interact, resulting in non-linear effects, often called as crowding or bubble swarm. The bubble swarm effect was proven to be important when the bubbly flow was operated at high gas phase fraction [19, 20, 21].

Besides the aspects mentioned earlier, the turbulence closure also needs to be addressed. It was proven that in certain cases the bubble induced turbulence (BIT) is critical. The presence of bubbles modifies the structure of the liquid turbulence field and the production of shear induced turbulence which in turns modifies bubble distribution and break-up and coa-

lence processes. These bubbles act as a source of the BIT, causing turbulence generation in flows that would otherwise be laminar. In general, the BIT model includes source term in the turbulence transport equations to account the turbulence generated by the bubbles, and different modes have been developed [22, 23, 24, 25]. However, notwithstanding a certain amount of success, application of these BIT models was quite limited due to their strong dependence on experimental data. The knowledge of the BIT model, up to these days, is still not completely understood [26].

Although the governing equations in the E-E method is well organized. It is usually not possible to obtain the numerical solution if the equations are solved without any special numerical treatment. The equations were found to be ill-posed in regions of higher gas phase fractions (gas phase fraction $> 26\%$) and a grid restriction is usually employed on E-E method to avoid an ill-posed problem [27]. It is also shown by Panicker et al. [28] that the addition of a dispersion term ensures the hyperbolicity of the PDE, and prevents the non-physical instabilities in the predicted multiphase flows upon grid refinement. Apart from that, although the Rhie and Chow interpolation was used [29], it is well known that the collocated grid discretization admits checker-board solutions when strong body forces are presented [30]. All these numerical aspects need to be carefully handled to prevent stability problems.

In this work, the E-E method was used to investigate the bubbly flows. The governing equations of the E-E method were briefly discussed. The finite volume discretization procedure implemented in CFD code OpenFOAM-6 was presented. Sophisticated numerics were used to handle the stability and robustness problem. To the knowledge of the authors, these numerical technologies were unpublished but are able to provide a stable numerical framework. `reactingTwoPhaseEulerFoam`, as the solver in which the numerical technique was implemented, was used to simulate nine bubbly flow test cases selected from the literature consist of chemical, nuclear, bio-processing and metallurgical engineering. The effects of the drag force, non-drag forces, bubble induced turbulence, bubble swarm on the predicted

phase fraction distribution, gas holdup, liquid velocity and the turbulence variables were investigated. Conclusions are drawn and a general numerical settings are suggested. All the investigated test cases are open-sourced as Mendeley Data, which can be useful to those working on similar areas.

2. Equations and numerics

2.1. Governing equations

Within the Eulerian framework, two sets of Navier-Stokes equations are ensemble-averaged, and the effects of turbulence and inter-phase phenomena are taken into account using closure models. The continuity equation, momentum equation, and energy equation in the E-E method are conditionally averaged by multiplying I_ϕ and then applying a conventional averaging technique, density weighted or otherwise. The current work focuses on the numerical treatment of the E-E method in CFD simulations for bubbly flows. Hence, the heat transfer and mass transfer are neglected here. Under such assumption, the conservation of mass for phase a and phase b can be expressed by [31] :

$$\frac{\partial (\alpha_a \rho_a)}{\partial t} + \nabla \cdot (\alpha_a \rho_a \mathbf{U}_a) = 0, \quad (1)$$

$$\frac{\partial (\alpha_b \rho_b)}{\partial t} + \nabla \cdot (\alpha_b \rho_b \mathbf{U}_b) = 0, \quad (2)$$

where α_a and α_b are the phase fraction of phase a and phase b , ρ_a and ρ_b are the density for phase a and phase b , and \mathbf{U}_a and \mathbf{U}_b are the average velocity for phase a and phase b , respectively. The average velocities \mathbf{U}_a and \mathbf{U}_b can be calculated by solving the corresponding phase momentum equations [31]:

$$\frac{\partial (\alpha_a \rho_a \mathbf{U}_a)}{\partial t} + \nabla \cdot (\alpha_a \rho_a (\mathbf{U}_a \otimes \mathbf{U}_a)) - \nabla \cdot (\alpha_a \rho_a \boldsymbol{\tau}_a) = -\alpha_a \nabla p_a + \alpha_a \rho_a \mathbf{g} - \mathbf{M}, \quad (3)$$

$$\frac{\partial (\alpha_b \rho_b \mathbf{U}_b)}{\partial t} + \nabla \cdot (\alpha_b \rho_b (\mathbf{U}_b \otimes \mathbf{U}_b)) - \nabla \cdot (\alpha_b \rho_b \boldsymbol{\tau}_b) = -\alpha_b \nabla p_b + \alpha_b \rho_b \mathbf{g} + \mathbf{M}, \quad (4)$$

where p_a and p_b are the pressure for each phase, τ_a and τ_b are the effective Reynolds stress tensors, \mathbf{g} is the gravitational acceleration vector, and \mathbf{M} is the interfacial force exchange term. It is common to break it down into the axial drag force \mathbf{M}_{drag} ; the lateral lift force \mathbf{M}_{lift} , which acts perpendicular to the direction of the relative motion of the two phases [32]; the wall lubrication force \mathbf{M}_{wall} which acts to drive the bubble away from the wall [33]; and the turbulent dispersion force \mathbf{M}_{turb} , which is the result of the turbulent fluctuations of the liquid velocity [34]. Specifically, the drag force can be calculated as follows:

$$\mathbf{M}_{\text{drag}} = \frac{3}{4} \alpha_a \rho_b C_D \frac{1}{d_a} |\mathbf{U}_b - \mathbf{U}_a| (\mathbf{U}_b - \mathbf{U}_a), \quad (5)$$

where C_D is the drag force coefficient and d_a is the diameter of phase a . The lift force can be calculated as follows [35]:

$$\mathbf{M}_{\text{lift}} = \alpha_b C_L \rho_a \mathbf{U}_r \times (\nabla \times \mathbf{U}_b), \quad (6)$$

where C_L is the lift force coefficient, \mathbf{U}_r is the relative velocity which equals $\mathbf{U}_b - \mathbf{U}_a$. The wall lubrication force can be calculated as follows [33]:

$$\mathbf{M}_{\text{wall}} = C_{\text{wall}} \rho_b \alpha_a |\mathbf{U}_r|^2 \cdot \mathbf{n}, \quad (7)$$

where C_{wall} is the wall lubrication force coefficient. The turbulence dispersion force can be calculated as follows [34]:

$$\mathbf{M}_{\text{turb}} = C_T \rho_b k_b \nabla \alpha_a, \quad (8)$$

where C_T is the turbulence dispersion force coefficient. A comprehensive discussion of the E-E method can be found in other latest work [36, 37].

The Reynolds stress, τ_a and τ_b , arises in the momentum equations as a result of the averaging process. Different turbulence models can be employed to calculate the Reynolds stress, such as the $k - \varepsilon$ model [38] and the $k - \omega$ SST model [39]. It was shown that

the $k - \omega$ turbulence model yielded a better qualitative prediction of the bubble plume than the $k - \varepsilon$ model, due to the low Reynolds number treatment of the former model [40]. Some other works showed that the $k - \varepsilon$ model can still yield good results for bubbly flows [41, 42]. Here the equations of the turbulence models are omitted for brevity and readers are referred to other works for more details [43]. However, it should be noted that in general the bubble induced turbulence (BIT) plays an important role. The presence of bubbles modifies the structure of the liquid turbulence field and the production of shear induced turbulence, which in turns modifies the bubble distribution and the break-up and coalescence processes. These bubbles act as a source of the BIT, also generating turbulence in flows that would otherwise be laminar. It is common practise for the BIT model to include a source term in the turbulence transport equations to account for the turbulence generated by the bubbles, and different BIT models have been developed [22, 44, 23, 24, 25]. Readers are suggested to other work for a comprehensive discussion [26].

It can be seen that the equations of the E-E method is well organized. However, analytical solutions can be hardly obtained due to the complex mathematical features of the partial differential equation. The numerical aspects of the equations are listed as follows:

- Singular problem arises in the phase momentum equation when one phase fraction approaches zero. To address the singular problem, previous studies used a non-conservative formulation after dividing by the phase fraction [45, 46]. Fully conservative formulation can also be applied [47].
- It is well known a checker-board distribution of the pressure arises if a collocated grid was used under the finite volume framework. This problem can be handled by using the Rhie and Chow interpolation [29]. Similarly, the gradient term (e.g., the turbulence dissipation term) at the R.H.S. of the phase momentum equation can introduce oscillating problems.
- High gas phase fraction near the wall can be predicted due to the lateral forces exerted

on small bubbles. The over-prediction of the gas phase fraction is non-physical and comes from the calculation of the gradient since no wall function model exists for the non-drag forces. A damping coefficient based on the ratio of the particle size to the distance to the wall needs to be used to damp the lateral force to prevent such over-predictions [48].

- Spurious currents arises when the mesh is highly non-orthogonal. Rather than solving the static pressure p , it is possible to solve p_{rgh} which equals $p - \rho \mathbf{g} \cdot \mathbf{h}$. This change is developed by Weller to avoid deficiencies in the handling of the pressure/buoyant force balance on non-orthogonal and distorted meshes [49]. Subtracting the hydrostatic part of the pressure can solve the problem of the interaction between the buoyancy force and non-orthogonality in regions of uniform density. Moreover, the specification of the pressure boundary condition is also simplified.

Readers are referred to the our previous work for a comprehensive discussion of the finite volume discretization of the equations in the E-E method [50]. In the following, we discuss the updated numerical techniques implemented in OpenFOAM-6.

2.2. Poisson equation for p_{rgh}

In order to prevent the wiggling distribution of the pressure, it is generally suggested to employ the semi-implicit algorithm following the spirit of Rhie and Chow interpolation [29]. After omitting the buoyancy and pressure terms, Eq. (1) and (2) can be written as follows:

$$\frac{\partial (\alpha_a \rho_a \mathbf{U}_a)}{\partial t} + \nabla \cdot (\alpha_a \rho_a (\mathbf{U}_a \otimes \mathbf{U}_a)) - \nabla \cdot (\alpha_a \rho_a \tau_a) = -\mathbf{KdU}_a - \mathbf{M}_{\text{lift}} - \mathbf{M}_{\text{turb}} - \mathbf{M}_{\text{wall}}, \quad (9)$$

$$\frac{\partial (\alpha_b \rho_b \mathbf{U}_b)}{\partial t} + \nabla \cdot (\alpha_b \rho_b (\mathbf{U}_b \otimes \mathbf{U}_b)) - \nabla \cdot (\alpha_b \rho_b \tau_b) = -\mathbf{KdU}_b + \mathbf{M}_{\text{lift}} + \mathbf{M}_{\text{turb}} + \mathbf{M}_{\text{wall}}, \quad (10)$$

where

$$\mathbf{Kd} = \frac{3}{4} \alpha_b \rho_b C_D \frac{1}{d_b} |\mathbf{U}_a - \mathbf{U}_b|. \quad (11)$$

It can be seen that only the negative $-\mathbf{KdU}_a$ and $-\mathbf{KdU}_b$ (part of the drag force contribution) are included in Eq. (9) and Eq. (10) since the negative coefficients can improve the diagonally dominant properties of the implicitly discretized momentum equation. The discretized form of Eq. (9) and (10) can be written as follows:

$$A_{a,P}\mathbf{U}_{a,P} + \sum A_{a,N}\mathbf{U}_{a,N} = S_{a,P}, \quad (12)$$

$$A_{b,P}\mathbf{U}_{b,P} + \sum A_{b,N}\mathbf{U}_{b,N} = S_{b,P}, \quad (13)$$

where the subscript P denotes the owner cell, the subscript N denotes the neighbour cells, A_P denotes the matrix diagonal coefficients contributed by the owner cells, A_N denotes the matrix coefficients contributed by the neighbour cells, and S denotes the source terms.

The predicted velocities can be obtained by solving the discretized form of Eq. (12) and (13), which can be written as follows:

$$\mathbf{HbyA}_{a,P} = \frac{1}{A_{a,P}}(-\sum A_{a,N}\mathbf{U}_{a,N} + S_{a,P}), \quad (14)$$

$$\mathbf{HbyA}_{b,P} = \frac{1}{A_{b,P}}(-\sum A_{b,N}\mathbf{U}_{b,N} + S_{b,P}), \quad (15)$$

where $\mathbf{HbyA}_{a,P}$ and $\mathbf{HbyA}_{b,P}$ denote the predicted velocities for phase a and phase b , respectively. At this stage, the predicted velocity fields are not divergence free. Therefore, following the spirit of the pressure-velocity coupling procedure [51], the pressure Poisson equation should be established and solved several times to correct the velocity. It should be noted that necessary numerical treatments are needed when the pressure Poisson equation is constructed. In the E-E method, it is common to assume an average pressure p to construct one pressure equation [52]. Moreover, in order to simplify the designation of the pressure boundary conditions and to reduce the spurious currents caused by hydrostatic pressure in the non-orthogonal grids, the pressure term and buoyancy term are usually combined

together, and the pressure without the hydrostatic part, p_{rgh} , is used. p_{rgh} is defined by

$$p_{\text{rgh}} = p - \rho \mathbf{g} \cdot \mathbf{h}, \quad (16)$$

where \mathbf{g} is the gravity vector and \mathbf{h} is the locations vector. The gradient of p_{rgh} can be written by

$$\nabla p_{\text{rgh}} = \nabla p - \rho \mathbf{g} - \mathbf{g} \cdot \mathbf{h} \nabla \rho, \quad (17)$$

Substituting Eq. (16) and Eq. (17) into the buoyance and pressure terms leads to:

$$\begin{aligned} -\alpha_a \nabla p + \alpha_a \rho_a \mathbf{g} &= -\alpha_a \nabla p_{\text{rgh}} - \alpha_a \rho \mathbf{g} - \alpha_a \mathbf{g} \cdot \mathbf{h} \nabla \rho + \alpha_a \rho_a \mathbf{g} \\ &= \alpha_a \nabla p_{\text{rgh}} - \alpha_b \alpha_a (\rho_b - \rho_a) \mathbf{g} - \alpha_a \mathbf{g} \cdot \mathbf{h} \nabla \rho, \end{aligned} \quad (18)$$

$$\begin{aligned} -\alpha_b \nabla p + \alpha_b \rho_b \mathbf{g} &= -\alpha_b \nabla p_{\text{rgh}} - \alpha_b \rho \mathbf{g} - \alpha_b \mathbf{g} \cdot \mathbf{h} \nabla \rho + \alpha_b \rho_b \mathbf{g} \\ &= \alpha_b \nabla p_{\text{rgh}} - \alpha_a \alpha_b (\rho_a - \rho_b) \mathbf{g} - \alpha_b \mathbf{g} \cdot \mathbf{h} \nabla \rho, \end{aligned} \quad (19)$$

where $-\alpha_b \nabla p_{\text{rgh}}$ and $-\alpha_a \nabla p_{\text{rgh}}$, together with the continuity equation, can be used to construct the pressure Poisson equation.

In order to address the possible large phase density difference in compressible flows, the density should be separated from the continuity equation as reported in Eq. (3) and (4). In this formulation the density terms can be seen as correction terms. The re-formulated continuity equations can be written as follows:

$$\frac{\partial \alpha_a}{\partial t} + \nabla \cdot (\alpha_a \mathbf{U}_a) = -\frac{\alpha_a}{\rho_a} \frac{D \rho_a}{Dt}, \quad (20)$$

$$\frac{\partial \alpha_b}{\partial t} + \nabla \cdot (\alpha_b \mathbf{U}_b) = -\frac{\alpha_b}{\rho_b} \frac{D \rho_b}{Dt}, \quad (21)$$

where $\frac{D}{Dt}$ denotes the material derivative. Summarizing Eq. (20) and Eq. (21) produces the

divergence constraint equation:

$$\nabla \cdot (\alpha_b \mathbf{U}_b + \alpha_a \mathbf{U}_a) = -\frac{\alpha_b}{\rho_b} \frac{D\rho_b}{Dt} - \frac{\alpha_a}{\rho_a} \frac{D\rho_a}{Dt}. \quad (22)$$

The R.H.S. of Eq. (22) represents the correction of the compressible term of $\nabla \cdot \mathbf{U} = 0$ (which is different from the traditional compressible algorithm) due to possible large density difference in two-phase flow. In this work, the compressible terms are neglected and we only discuss the incompressible terms. For the incompressible terms, the discretized form of Eq. (22) can be written as follows:

$$\sum (\alpha_{a,f} \mathbf{U}_{a,f} + \alpha_{b,f} \mathbf{U}_{b,f}) \cdot \mathbf{S}_f = 0. \quad (23)$$

In case of convergence, the velocities should satisfy the divergence constraint as reported in Eq. (23). It is usually employed as a restrictive condition which can be used to construct pressure Poisson equation. Specifically, in Eq. (14) and (15), the pressure gradient and buoyancy term are not considered to update the predicted velocity. After adding the effect of the buoyancy and pressure gradient, the predicted velocity can be written as

$$\mathbf{U}_{a,p} = \mathbf{H} \mathbf{b}_y \mathbf{A}_{a,P} + \frac{\alpha_{a,P}}{\mathbf{A}_{a,P}} (\nabla p_{\text{rgh},P} - \alpha_{b,P} (\rho_b - \rho_a) \mathbf{g} - \mathbf{g} \cdot \mathbf{h}_P \nabla \rho_P) + \frac{K d_P}{\mathbf{A}_{a,P}} \mathbf{U}_{b,P}, \quad (24)$$

$$\mathbf{U}_{b,p} = \mathbf{H} \mathbf{b}_y \mathbf{A}_{b,P} + \frac{\alpha_{b,P}}{\mathbf{A}_{b,P}} (\nabla p_{\text{rgh},P} - \alpha_{a,P} (\rho_a - \rho_b) \mathbf{g} - \mathbf{g} \cdot \mathbf{h}_P \nabla \rho_P) + \frac{K d_P}{\mathbf{A}_{b,P}} \mathbf{U}_{a,P}, \quad (25)$$

Substituting the interpolated cell face velocities into Eq. (23), the phase flux can be written as follows:

$$\alpha_{b,f} \phi_b + \alpha_{a,f} \phi_a = \nabla \cdot \left(\left(\alpha_{b,P} \frac{\alpha_{b,P}}{\mathbf{A}_{b,P}} + \alpha_{a,P} \frac{\alpha_{a,P}}{\mathbf{A}_{a,P}} \right) \nabla p_{\text{rgh},P} \right), \quad (26)$$

where

$$\phi_a = (\mathbf{H} \mathbf{b}_y \mathbf{A}_{a,f} + \frac{\alpha_{a,f}}{\mathbf{A}_{a,f}} (-\alpha_{b,f} (\rho_b - \rho_a) \mathbf{g} - \mathbf{g} \cdot \mathbf{h}_f \nabla \rho_f) + \frac{K d_f}{\mathbf{A}_{a,f}} \mathbf{U}_{b,f}) \cdot \mathbf{S}_f, \quad (27)$$

$$\phi_b = (\mathbf{H}\mathbf{b}\mathbf{y}\mathbf{A}_{b,f} + \frac{\alpha_{b,f}}{\mathbf{A}_{b,f}}(-\alpha_{a,f}(\rho_a - \rho_b)\mathbf{g} - \mathbf{g} \cdot \mathbf{h}_f \nabla \rho f) + \frac{\mathbf{Kd}_f}{\mathbf{A}_{b,f}}\mathbf{U}_{a,f}) \cdot \mathbf{S}_f. \quad (28)$$

Eq. (26), Eq. (24) and (25) can be employed in the PISO algorithm [51] to obtain divergence-free velocities.

2.3. Relative velocity formulation

When the drag coefficient \mathbf{Kd} is much larger than the diagonal coefficient \mathbf{A} at certain cells, the classical semi-implicit algorithm discussed previously leads to very large relative velocity Courant number. It will cause convergence problem and the time step will be very small. In OpenFOAM-6, another more robust approach was implemented by Weller to handle the pressure-velocity coupling [49], which will be called Weller method in the following sections. This method is similar to the partial elimination method (PEM) developed by Spalding [53]. Both methods increase the stability by manipulating the relative phase velocity formulation. In Weller method, the velocities without contributions of the drag forces are defined as follows:

$$\mathbf{U}_{a,p}^s = \mathbf{H}\mathbf{b}\mathbf{y}\mathbf{A}_{a,p} + \frac{\alpha_{a,p}}{\mathbf{A}_{a,p}}(\nabla p_{\text{rgh},p} - \alpha_{b,p}(\rho_b - \rho_a)\mathbf{g} - \mathbf{g} \cdot \mathbf{h}_p \nabla \rho p), \quad (29)$$

$$\mathbf{U}_{b,p}^s = \mathbf{H}\mathbf{b}\mathbf{y}\mathbf{A}_{b,p} + \frac{\alpha_{b,p}}{\mathbf{A}_{b,p}}(\nabla p_{\text{rgh},p} - \alpha_{a,p}(\rho_a - \rho_b)\mathbf{g} - \mathbf{g} \cdot \mathbf{h}_p \nabla \rho p). \quad (30)$$

The phase velocities can be written as

$$\mathbf{U}_{a,p} = \mathbf{U}_{a,p}^s + D_{a,p}\mathbf{U}_{b,p} \quad (31)$$

$$\mathbf{U}_{b,p} = \mathbf{U}_{b,p}^s + D_{b,p}\mathbf{U}_{a,p} \quad (32)$$

$$\mathbf{U}_p = \alpha_{b,p}(\mathbf{U}_{b,p}^s + D_{b,p}\mathbf{U}_{a,p}) + \alpha_{a,p}(\mathbf{U}_{a,p}^s + D_{a,p}\mathbf{U}_{b,p}) \quad (33)$$

where $D_{b,p} = \frac{\mathbf{Kd}_p}{\mathbf{A}_{b,p}}$, $D_{a,p} = \frac{\mathbf{Kd}_p}{\mathbf{A}_{a,p}}$. The relative velocity is defined by

$$\mathbf{U}_p^r = \mathbf{U}_{b,p} - \mathbf{U}_{a,p} = \mathbf{U}_{b,p}^s + D_{b,p}\mathbf{U}_{a,p} - \mathbf{U}_{a,p}^s - D_{a,p}\mathbf{U}_{b,p}. \quad (34)$$

Subtracting $D_{b,P}D_{a,P}(\mathbf{U}_{b,P} - \mathbf{U}_{a,P})$ from the L.H.S. and the R.H.S. of Eq. (34) leads to:

$$\begin{aligned} \mathbf{U}_P^r - D_{b,P}D_{a,P}(\mathbf{U}_{b,P} - \mathbf{U}_{a,P}) = \\ \mathbf{U}_{b,P}^s + D_{b,P}\mathbf{U}_{a,P} - \mathbf{U}_{a,P}^s - D_{a,P}\mathbf{U}_{b,P} - D_{b,P}D_{a,P}(\mathbf{U}_{b,P} - \mathbf{U}_{a,P}). \end{aligned} \quad (35)$$

After arrangement, Eq. (35) can be written as

$$\mathbf{U}_P^r = \frac{(1 - D_{a,P})\mathbf{U}_{b,P}^s - (1 - D_{b,P})\mathbf{U}_{a,P}^s}{1 - D_{a,P}D_{b,P}}. \quad (36)$$

Once the relative velocity \mathbf{U}_P^r is updated, the velocity of discrete phase and continuous phase can be calculated by the following equations, respectively:

$$\mathbf{U}_{a,P} = \mathbf{U}_P - \alpha_{b,P}\mathbf{U}_P^r, \quad (37)$$

$$\mathbf{U}_{b,P} = \mathbf{U}_P + \alpha_{a,P}\mathbf{U}_P^r. \quad (38)$$

It can be seen that the difference between the Weller method (Eq. (36)) with the traditional method (Eq. (34)) is the methodology of calculating the relative velocity. If the drag coefficient is larger than the diagonal coefficient ($D \gg 1$), the relative velocity obtained by the traditional algorithm degenerates to:

$$\mathbf{U}_{b,P}^r = D_{b,P}\mathbf{U}_{a,P} - D_{a,P}\mathbf{U}_{b,P}. \quad (39)$$

On the other hand, the relative velocity calculated by the Weller method degenerates to:

$$\mathbf{U}_{b,P}^r = \frac{1}{D_{b,P}}\mathbf{U}_{a,P}^s - \frac{1}{D_{a,P}}\mathbf{U}_{b,P}^s. \quad (40)$$

Obviously, the relative velocity calculated by Weller method won't lead to spurious relative velocity Courant number.

2.4. Numerical treatment for strong body forces

For the flows with strong swirl or strong body forces, the algorithm discussed above tends to produce phase fraction oscillations [30]. For example, in vertical pipe flows where the lift, dispersion and wall lubrication forces are strong, the phase fraction oscillations occurs frequently. Following the spirit of the Rhie and Chow interpolation [29], this issue can be mitigated by including these body forces on the cell faces to construct the pressure equation, instead of being discretized in the velocity equations as reported in Eq. (9) and Eq. (10). Therefore, Eq. (9) and Eq. (10) can be re-written as follows:

$$\frac{\partial (\alpha_a \rho_a \mathbf{U}_a)}{\partial t} + \nabla \cdot (\alpha_a \rho_a (\mathbf{U}_a \otimes \mathbf{U}_a)) - \nabla \cdot (\alpha_a \rho_a \tau_a) = -\mathbf{K} \mathbf{d} \mathbf{U}_a, \quad (41)$$

$$\frac{\partial (\alpha_b \rho_b \mathbf{U}_b)}{\partial t} + \nabla \cdot (\alpha_b \rho_b (\mathbf{U}_b \otimes \mathbf{U}_b)) - \nabla \cdot (\alpha_b \rho_b \tau_b) = -\mathbf{K} \mathbf{d} \mathbf{U}_b. \quad (42)$$

It can be seen that in Eq. (41) and Eq. (42) the contribution of the non-drag forces is neglected. The contribution needs to be considered to update the predicted velocities. Therefore, Eq. (24) and Eq. (25) can be re-written as follows:

$$\begin{aligned} \mathbf{U}_{a,p} = & \mathbf{H} \mathbf{b}_y \mathbf{A}_{a,P} + \frac{\alpha_{a,P}}{\mathbf{A}_{a,P}} (\nabla p_{\text{rgh},P} - \alpha_{b,P} (\rho_b - \rho_a) \mathbf{g} - \mathbf{g} \cdot \mathbf{h}_P \nabla \rho_P) \\ & + \frac{\mathbf{K} \mathbf{d}_P}{\mathbf{A}_{a,P}} \mathbf{U}_{b,P} - \mathbf{M}_{\text{lift},P} - \mathbf{M}_{\text{turb},P} - \mathbf{M}_{\text{wall},P}, \end{aligned} \quad (43)$$

$$\begin{aligned} \mathbf{U}_{b,p} = & \mathbf{H} \mathbf{b}_y \mathbf{A}_{b,P} + \frac{\alpha_{b,P}}{\mathbf{A}_{b,P}} (\nabla p_{\text{rgh},P} - \alpha_{a,P} (\rho_a - \rho_b) \mathbf{g} - \mathbf{g} \cdot \mathbf{h}_P \nabla \rho_P) \\ & + \frac{\mathbf{K} \mathbf{d}_P}{\mathbf{A}_{b,P}} \mathbf{U}_{a,P} + \mathbf{M}_{\text{lift},P} + \mathbf{M}_{\text{turb},P} + \mathbf{M}_{\text{wall},P}, \end{aligned} \quad (44)$$

The corresponding flux can be written as

$$\begin{aligned} \phi_a = & (\mathbf{H} \mathbf{b} \mathbf{y} \mathbf{A}_{a,f} + \frac{\alpha_{a,f}}{\mathbf{A}_{a,f}} (-\alpha_{b,f}(\rho_b - \rho_a) \mathbf{g} - \mathbf{g} \cdot \mathbf{h}_f \nabla \rho_f) + \frac{K d_f}{\mathbf{A}_{a,f}} \mathbf{U}_{b,f}) \cdot \mathbf{S}_f \\ & - (\mathbf{M}_{\text{lift,P}} + \mathbf{M}_{\text{turb,P}} + \mathbf{M}_{\text{wall,P}}) \cdot \mathbf{S}_f, \quad (45) \end{aligned}$$

$$\begin{aligned} \phi_b = & (\mathbf{H} \mathbf{b} \mathbf{y} \mathbf{A}_{b,f} + \frac{\alpha_{b,f}}{\mathbf{A}_{b,f}} (-\alpha_{a,f}(\rho_a - \rho_b) \mathbf{g} - \mathbf{g} \cdot \mathbf{h}_f \nabla \rho_f) + \frac{K d_f}{\mathbf{A}_{b,f}} \mathbf{U}_{a,f}) \cdot \mathbf{S}_f \\ & + (\mathbf{M}_{\text{lift,P}} + \mathbf{M}_{\text{turb,P}} + \mathbf{M}_{\text{wall,P}}) \cdot \mathbf{S}_f, \quad (46) \end{aligned}$$

Substituting ϕ_a and ϕ_b into Eq. (26) leads to the pressure Poisson equation which can prevent the oscillating results coming from the strong body forces.

3. Test cases

As previously mentioned, the lack of an ideal experiment, with a good mix of local and global measurements performed under a wide spectrum of operating conditions, necessary for a complete model validation, brought us to consider many different test cases with different geometries. These test cases were selected from different works. The schematic representation of these test cases is reported in Fig. 1. All of them were investigated by experiments which implies they are suitable benchmark test cases for numerical investigations. Moreover, they were observed with different features which are listed as follows:

- Test case A.1: investigation of bubble plumes in a rectangular bubble column of Díaz et al. [54]. The experimental equipment consists of a 0.2 m wide, 1.8 m high and 0.04 m deep partially aerated bubble column, filled with tap water up to 0.45 m from the bottom at room temperature and atmospheric pressure, while the air is fed through a sparger composed of eight centered holes of 1 mm of diameter and 6 mm pitch. This test case was proven to be a very interesting test case because the liquid vortices generated by the bubble plumes are a favorable factor for mixing and, therefore,

for speeding up all transport processes [55]. Additionally, the existence of flow structures showing unsteady liquid recirculation is a typical phenomenon in industrial-scale bubble columns.

- Test case A.2: investigation of gas-liquid flows in an industrial bubble column of McClure et al. [56]. It is a partially aerated cylindrical bubble column of 0.19 m diameter with a multi-point sparger filled with water up to 1 m from the bottom. The aspect ratio (L/D) is about 5. In the bio-processing industry, the bubble column height to diameter typically ranges from 2 to 5 and is usually operated in the heterogeneous flow regime to speed up mass and heat transfer. Meanwhile, the state-state solution can be hardly obtained due to large superficial velocity and high gas holdup.
- Test case A.3: investigation of sudden enlargement pipe flow of Bel F'dhila [57]. The test case studied here is that of a bubbly air/water upward flow through a pipe with a sudden enlargement. The diameters of the two pipe sections are 50 mm and 100 mm, respectively. The inlet phase fraction is characterised by a wall peak in experiments. The feature of this test case is that there is a large separation zone at the bottom of the pipe. This case has been employed extensively to verify the E-E method and implementation [58, 59, 60, 61].
- Test case B.1: investigation of bubbly flow in a cylindrical pipe of Lucas et al. [62]. Mixture of the gas and liquid is injected from the bottom pipe of 0.0256 m diameter and 3.53 m height. For the vertical upward flow smaller bubbles tend to move towards the wall. A wall peak of the gas phase fraction occurs at the position of high L/D . This was also observed for single bubbles by Tomiyama et al. [63]. In the case of vertical co-current pipe flow the radial flow field is symmetrically stable over a long distance. Therefore, this type of flow is well suited for the investigation of the non-drag forces.
- Test case B.2: investigation of bubbly flow in a circular pipe of Banowski et al. [64]. The experiment comprises a vertical pipe with 54.8 mm inner diameter and 6 m length.

Gas and liquid mixture is injected from the bottom. It is similar with the test case B.2. However, besides the typical wall peak formed due to the smaller bubbles movement, a double peak of the phase fraction can also be observed due to the existence of large bubbles because the large bubbles tend to move to the center.

- Test case B.3: investigation of bubbly flow in a rectangle pipe of Žun [65]. This test case is similar with test case B.3 with slightly difference of the geometry. Mixture of the gas and liquid is injected from the bottom of a rectangle channel of 0.0254 m length and 2 m height. Central peak and double peak of the gas phase fraction were observed.
- Test case B.4: investigation of bubbly flow of Besagni et al. [66]. The gas-liquid flow in an annular gap bubble column with two non-regular internal pipes was investigated. It consists of a non-pressized vertical column with an inner diameter 0.24 m and a height 5.3 m. In simulations the height of the domain is limited to 5 m. Two internal pipes are placed inside the column: one centrally positioned (with an external diameter of 0.06 m) and one asymmetrically positioned (with an external diameter of 0.075 m). The sparger is modeled as a uniform cylindrical surface with a height of 0.01 m placed on the lateral inner pipe at the vertical position of 0.3 m from the bottom of the domain. The aspect ratio of the geometry is small. Due to the existence of the non-irregular components, the gas phase fraction distribution developed to be quite flatten and no wall peak was observed in the experiments, even it can be seen as a pipe flow.
- Test case C.1: investigation of gas-liquid flows in a continuous casting molds of Iguchi and Kasai [67]. The geometry employed in this test case is quite different with previous ones. The gas and liquid is injected into a rectangular vessel of 0.3 m length and 0.15 m width. In the experiments, it was observed that larger bubbles are lifted towards the liquid surface due to the buoyancy force acting on them, while smaller bubbles are carried deep. Such phenomenon is also known as phase segregation or poly-dispercity

in other works, which was proven as a tough work for the E-E method.

- Test case C.2: investigation of gas-liquid flows in a continuous casting molds of Sheng and Irons [68]. The gas phase is injected from the bottom of the vessel of 0.76 m height and 0.5 m diameter. In this test case, the measured turbulence fields, gas phase fraction distribution, gas/liquid velocities in the plume zone were used for validation of various turbulence models. It can be seen as a suitable test case to validate the multi-phase turbulence model against experimental data.

The reader may find these test cases are sorted by different groups. The bubble columns investigated in test case A.1 - A.3 are mainly encountered in chemical and bio-processing engineering. The aspect ratio of the geometry is small. They are usually used to speed up mixing and heat/mass transfer and are typically operated in medium or high superficial velocity. A strong coupling between the disperse phase and continuous phase is observed. The local phase fraction may be high. Meanwhile, the liquid flow in these bubble columns is highly transient and full of chaos with large-scale vortices. The pipe flow investigated in test case B.1 - B.4 are mainly encountered in nuclear engineering process. The aspect ratio of these pipes are relatively large. Different flow types exist depending on the gas flow rate. Dilute bubbly flows are found when operated at low gas superficial velocity. In bubbly flows, the liquid flow is rather stable and a steady-state can be achieved. The shape of the phase fraction distribution develops gradually to a stable distribution along the pipe axial direction, since the aspect ratio is quite large which implies the gas phase has enough time to develop. The bubbly flows investigated in test case C.1 - C.2 are mainly encountered in metallurgical engineering. The scale of the gas-liquid reactor is the same with that employed in the chemical engineering. The aspect ratio is also small. However, non-irregular design is quite common and the flow field is complex due to the existence of the complex geometry. Meanwhile, the small bubbles in the liquid phase, due to the phase segregation movement, are usually seen as impurity which need to be removed. At last, it should be stressed that although these test cases coming from different industries are full of different features, the

core problem lies in the investigation of the gas-liquid flows by the numerical method.

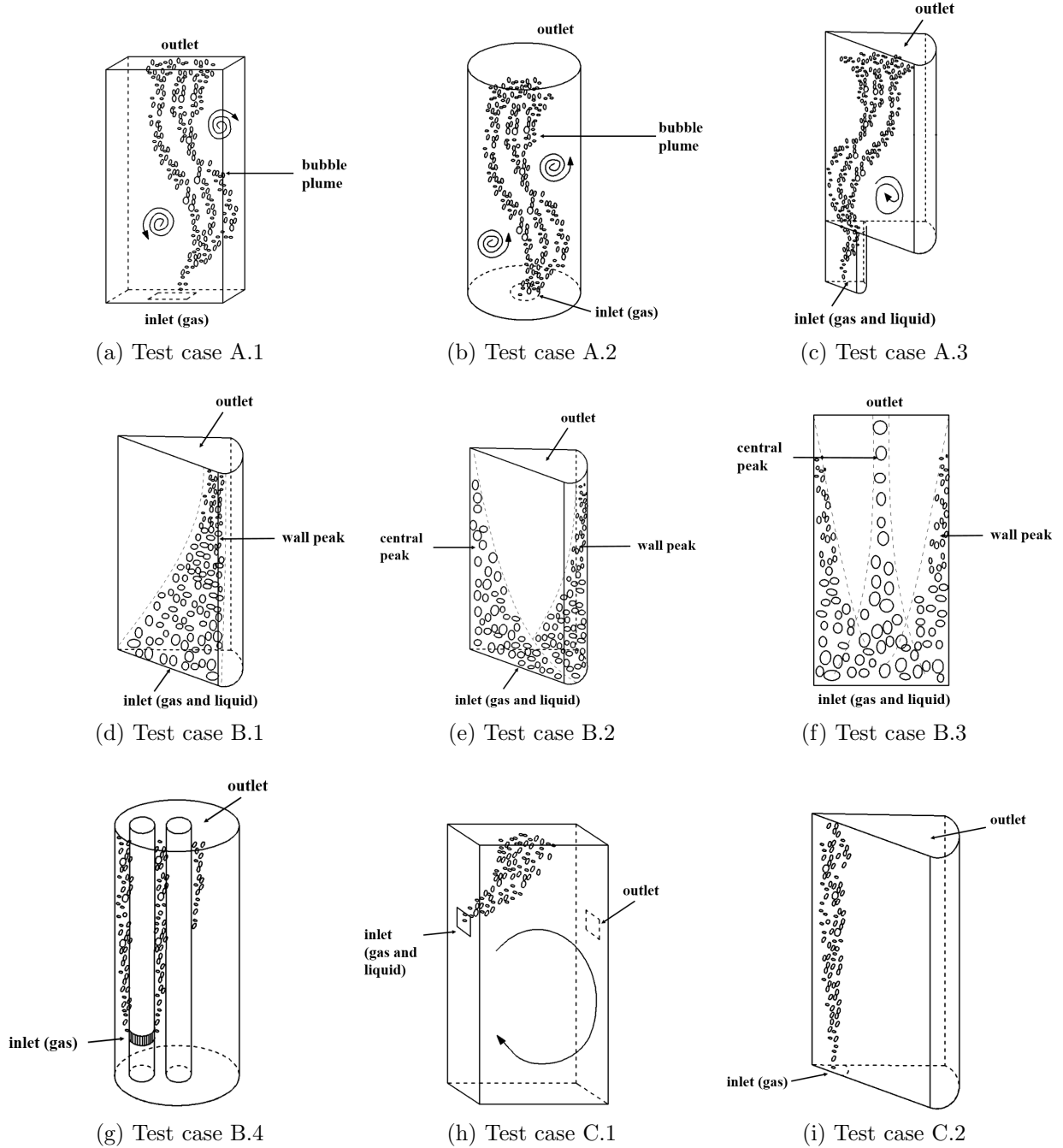


Figure 1: Schematic of the gas-liquid flows investigated in this work.

The computational grids employed in these test cases are shown in Fig. 2. 3D hexahedral cells were generated for test case A.1, A.2 and C.1. 2.5D axi-symmetric wedge cells were

employed for test case A.3, B.1, B.2 and C.2. 2D hexahedral cells were employed for test case B.3. Non-regular gambit-paving meshes was employed for test case B.4 due to the existence of the non-regular geometries. Our grid independence investigation, though not shown herein for brevity, suggested that the predicted results are not sensitive to the grid resolution. The base setup for these test cases are listed in Table 1 and 2. In our preliminary investigations such numerical setup compromises between stability and accuracy. Therefore, the remainder of the simulations in this study will utilize this base setup. The main boundary conditions are listed in Table 3. Since large amount test cases were employed in this work, it is not possible to document all the settings for brevity. Readers are referred to the source code of the test cases for further details.

At last, it should be stressed here that the combination of the drag force and turbulence dispersion force was used as default settings for all the test cases. The drag force, as the most important momentum exchange term, plays the most important role and addresses the coupling between the gas and liquid phase. The turbulence dispersion force should be included as well to address the pseudo-turbulence effect, otherwise the gas phase tends to accumulate locally, especially for those cases operated at pseudo-steady-state.

Term	Configuration
$\partial/\partial t$	Euler implicit
$\nabla\psi$	Gauss linear
∇p	Gauss linear
$\nabla \cdot (\psi \mathbf{U}\mathbf{U})$	Gauss limitedLinearV 1;
$\nabla \cdot (\mathbf{U}\psi)$	Gauss limitedLinear 1
$\nabla \cdot \boldsymbol{\tau}$	Gauss linear
$\nabla^2\psi$	Gauss linear uncorrected
$\nabla^\perp\psi$	uncorrected
ψ_f	linear

Table 1: Numerical configurations used in the test cases: ψ denotes a generic variable. $(\dots)_f$ is the face interpolation operator. ∇^\perp is the surface-normal gradient. The number “1” indicates the compliance of the scheme with the definition of TVD scheme. A value of 1 indicates full TVD compliance.

	Solver	Preconditioner	Rel. tol.	Final tol.
p	PCG	DIC	0.01	1e-7
k	PBiCGStab	DILU	-	1e-7
ε	PBiCGStab	DILU	-	1e-7

Table 2: Solvers and related settings used in the test cases.

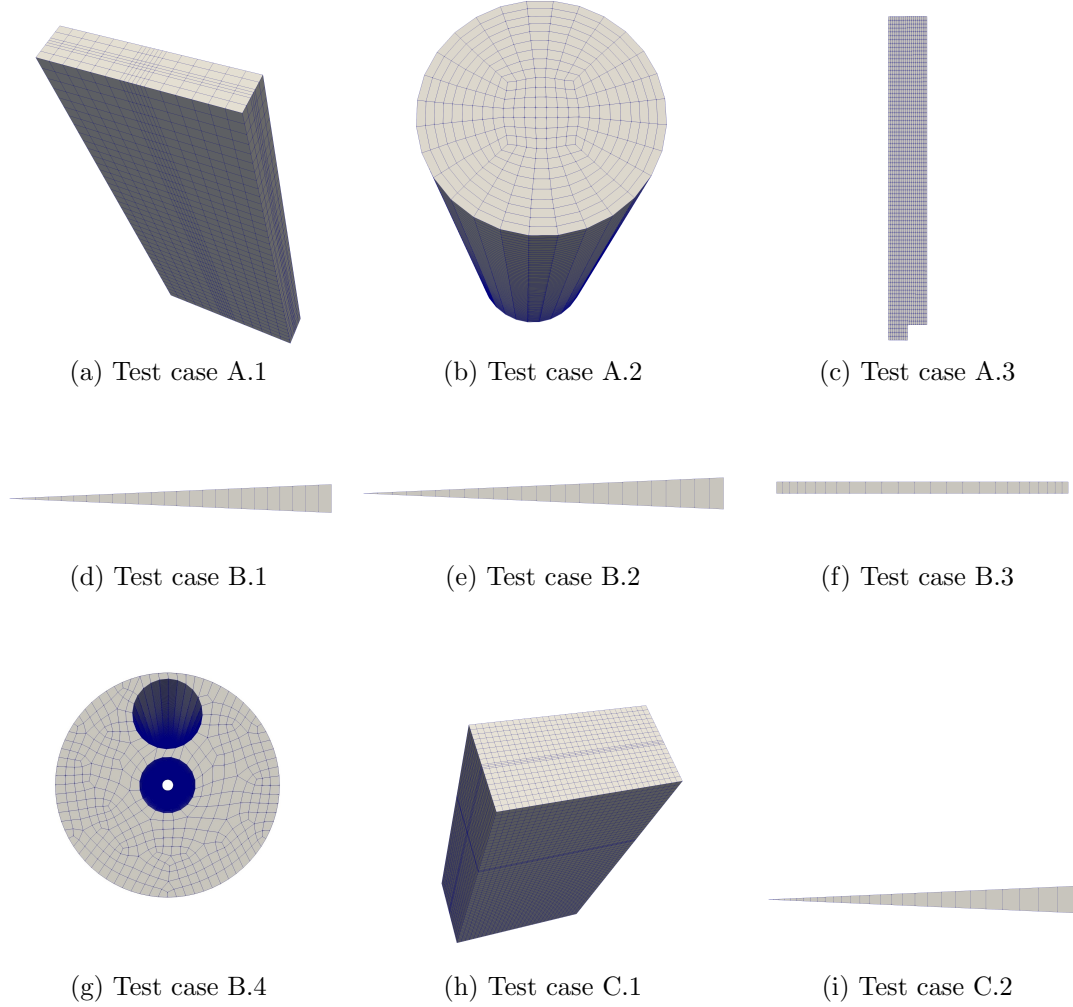


Figure 2: Computational grids employed for the test cases.

Test case	Operating conditions
A.1	Inlet gas velocity: 0.0024 m/s Inlet liquid velocity: 0 m/s Bubble diameter: 0.00505 m
A.2	Inlet gas velocity: 0.08 m/s Inlet liquid velocity: 0 m/s Bubble diameter: 0.005 m
A.3	Inlet gas velocity: 1.87 m/s Inlet liquid velocity: 1.57 m/s Bubble diameter: 0.02 m
B.1	Inlet gas velocity: 0.0115 m/s Inlet liquid velocity: 1.0167 m/s Bubble diameter: 0.0048 m
B.2	Inlet gas velocity: 0.0151 m/s Inlet liquid velocity: 1.017 m/s Bubble diameter: reported separately
B.3	Inlet gas velocity: 0.5 m/s Inlet liquid velocity: 0.43 m/s Bubble diameter: reported separately
B.4	Inlet gas velocity: 0.0087 m/s Inlet liquid velocity: 0 m/s Bubble diameter: 0.0042 m
C.1	Inlet gas velocity: 4 cm ³ /s Inlet liquid velocity: 5 l/s Bubble diameter: reported separately
C.2	Inlet gas velocity: 50 ml/s Inlet liquid velocity: 0 m/s Bubble diameter: 0.004 m
Gas velocity at walls: slip. Liquid velocity at walls: no-slip. k and ε at walls: wall function. Outlet: zero-gradient.	

Table 3: Main boundary conditions adopted in the simulations.

4. Results and discussions

4.1. Test case A.1 - A.3

In this section, the numerical predicted results for test case A.1 to A.3 were investigated. The available experimental data and features are listed in Table 4. These test cases are common in chemical and bio-processing engineering. In test case A.1, the gas phase was injected into the column at a relatively small superficial velocity. A “cooling tower” flow

regime was formed due to the existence of periodic large vortex. In test case A.2, the gas phase was injected into the cylinder column at high superficial velocities. The local gas phase fraction reached as high as 30%. The flow fields were highly transient and full of vortexes. In test case A.3, the gas phase was injected into a sudden enlargement pipe and a steady-state stagnant vortex was formed at the pipe bottom. In experiments, the turbulence kinetic energy was monitored, which can be used to validate the turbulence model employed in the E-E method.

Test case	Exp. data	Features	Pseudo-steady-state
A.1	Plume oscillating period Gas holdup	Periodic flow field	No
A.2	Phase frac. distri.	High phase fraction	No
A.3	Upward liquid vel. Turb. kinetic energy	Stagnant vortex	Yes

Table 4: Available experimental data and features of test case A.1 to A.3.

Fig. 3 and 4 show the horizontal liquid velocity predicted by different drag models for test case A.1. The turbulence dispersion model was also used. It can be seen that all these drag models can predict the periodically “Gulf-stream” phenomenon, which proves that the periodically vortex in the bubble column is not sensitive to the drag models. Table 5 shows the gas holdup and the plume oscillation period (POP) predicted by different momentum interfacial exchange terms. Compared with the experimental data, the POP predicted by Grace drag model was slightly better than those predicted by Schiller and Naumann (S-N) and Ishii and Zuber (I-Z) drag model. The effect of the addition of lift and turbulence dispersion force on the POP is negligible. It can be explained by the fact that the phase shear rate is too small to present differences. However, the addition of lift force and turbulence dispersion force improves the prediction of the gas holdup. Apart from that, it was found in our study that the effect of the BIT on the POP and gas holdup was negligible. Therefore, these results were not shown for brevity.

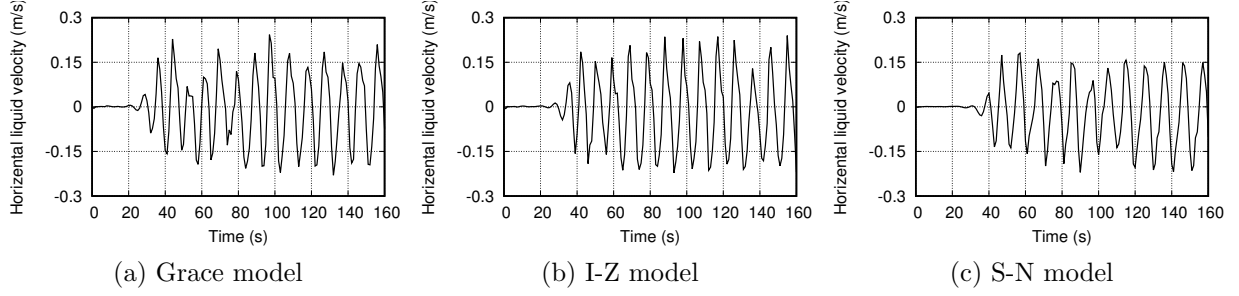


Figure 3: Horizontal liquid velocity predicted by different drag models for case A.1. $U_g = 0.0024$ m/s. Location: $x = 0.1$ m, $y = 0.225$ m, $z = 0.02$ m.

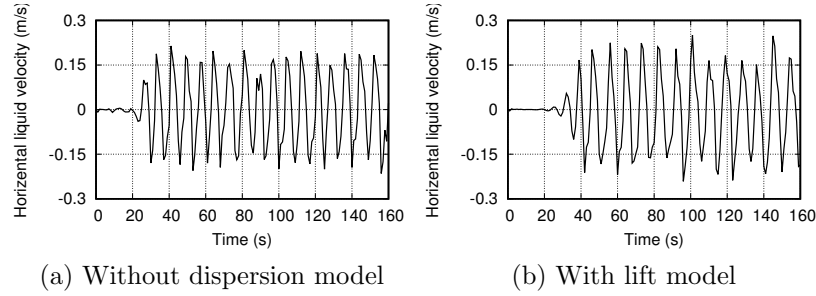


Figure 4: Horizontal liquid velocity predicted by Grace model with other momentum force terms for case A.1. $U_g = 0.0024$ m/s. Location: $x = 0.1$ m, $y = 0.225$ m, $z = 0.02$ m.

	Drag (SN)	Drag (IZ)	Drag (Grace)	Drag (Grace) & Lift	Drag (Grace) & Turb. disp.	Exp.
Gas holdup	0.00469	0.00613	0.00598	0.00644	0.00665	0.0069
Gas holdup rel. error	32%	11%	13%	6%	3%	-
POP	9.44	9.375	11.25	8.2	9.23	11.38

Table 5: Comparison of the gas holdup and POP predicted by different momentum exchange models with experimental data for test case A.1.

Fig. 5 shows the averaged phase fraction predicted by different drag models with and without bubble swarm correction. It can be seen that the phase fraction is directly dependent on the drag model. The phase fraction predicted by Grace and I-Z drag model were overestimated. It is because that the drag coefficient predicted by Grace and I-Z drag model is larger than that predicted by the S-N drag model. The addition of the bubble swarm

model by Tomiyama et al. [69] improves the predictions (bubble swarm coefficient is 1.0). It is consistent with the literature since it is common to consider bubble swarm effect when operated at high gas phase fraction [70, 19, 21, 20]. Fig. 6 shows the predicted averaged phase fraction when the Lahey BIT model and bubble swarm correction were included. It can be seen that the effect of the addition of the Lahey BIT model cannot improve the results for this test case.

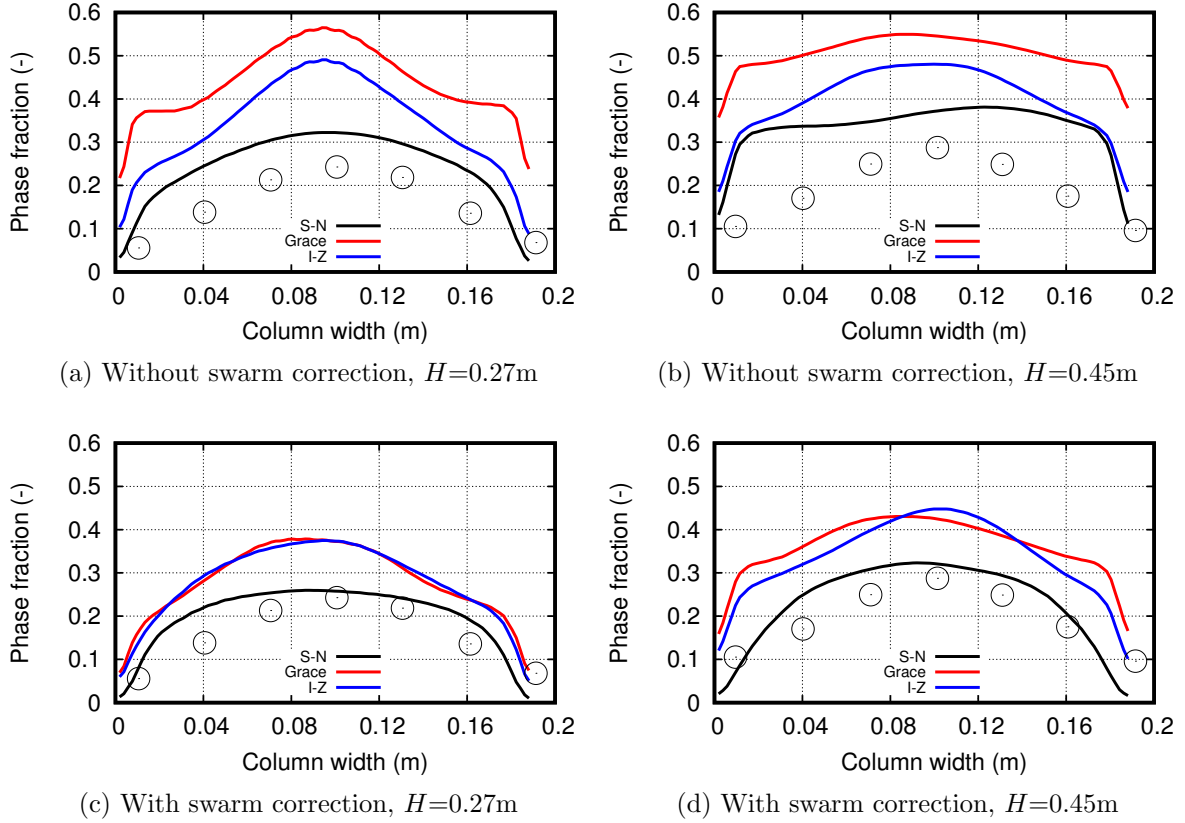


Figure 5: Comparison of the phase fraction (lines) predicted by different drag models with experimental data (circles). $U_g = 0.08$ m/s.

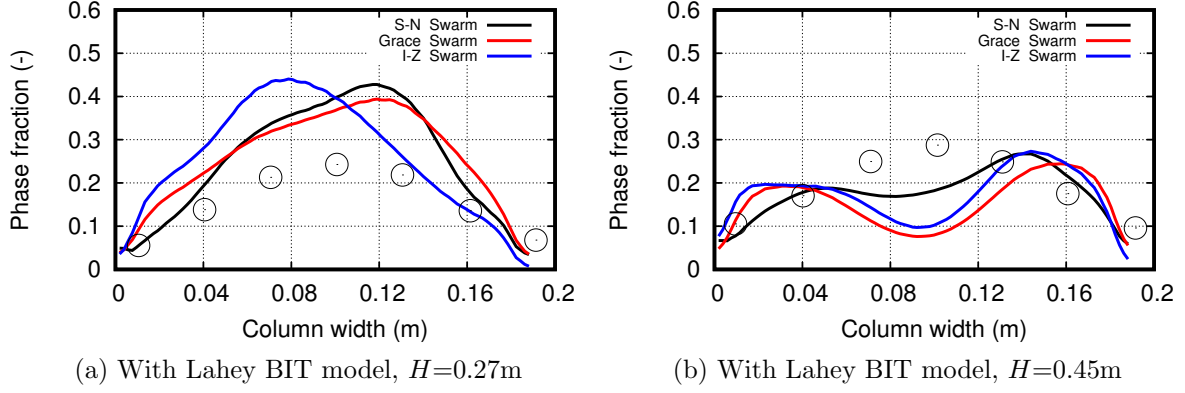


Figure 6: Comparison of the predicted phase fraction (lines) with experimental data (circles). Lahey BIT model and bubble swarm correction were used. $U_g = 0.08$ m/s.

To further investigate the BIT model, Fig. 7 shows the predicted mean axial liquid velocities with and without the BIT model for test case A.3. It can be seen that the velocities predicted by the Sato BIT model were similar with those when the BIT model was not included. Both of them agree well with experimental data. The axial liquid velocity predicted by the Lahey BIT model was slightly under-estimated, which can be explained by the over-predicted damping effect since the turbulent viscosity was over-predicted. Fig. 8 shows turbulent kinetic energy of the continuous phase for test case A.3. It can be seen that all the results were under-estimated by these models, even the mainstream velocities were correctly predicted. At present, this under-estimation cannot be explained with certainty, but evidence suggests that this may come from the inlet boundary conditions. In other works [58], the inlet boundary conditions was prescribed according to the measurements, in which a wall peak existed. Even by such settings, the turbulent kinetic energy was also under-estimated by certain turbulence models [58, 71], which proves the prediction of turbulence variables is a quite difficult task. In this study, a uniform inlet distribution without wall peak was assumed and the predictions were flattened. However, although the turbulent kinetic energy was under-estimated, it can be seen that the results predicted by the Lahey BIT model is even more flattened compared those predicted by Sato BIT model.

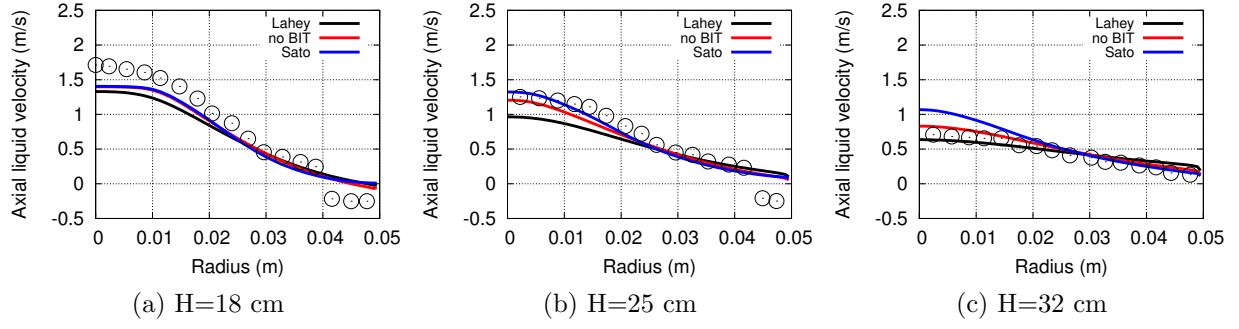


Figure 7: Predicted profiles of the mean axial liquid velocity (lines) compared with experimental data (circles) at different height for case A.3. Lahey: simulations by the Lahey BIT model. Sato: simulations by the Sato BIT model. No BIT: no BIT model was used.

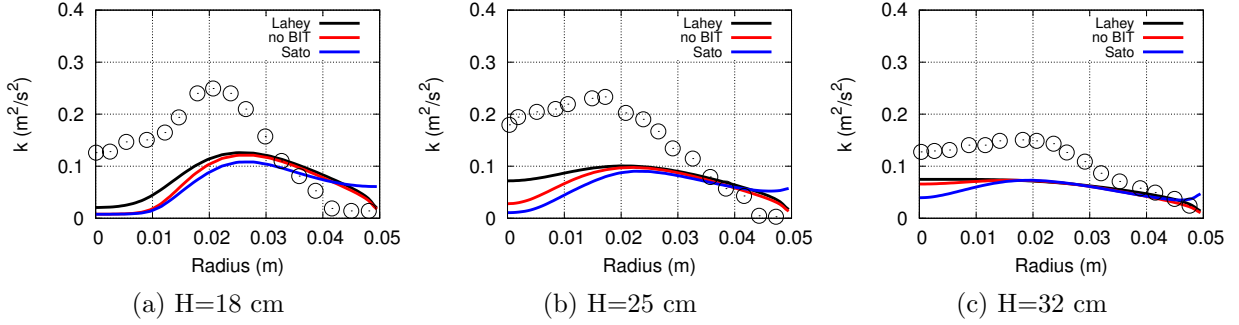


Figure 8: Predicted profiles of turbulent kinetic energy of the continuous phase (lines) compared with experimental data (circles) at different height for case A.3. Lahey: simulations by the Lahey BIT model. Sato: simulations by the Sato BIT model. No BIT: no BIT model was used.

4.2. Test case B.1 - B.4

In this section, the numerical predicted results for test case B.1 to B.4 were investigated. The available experimental data and features are listed in Table 6. These test cases are common in nuclear engineering. In test case B.1 to B.3, the aspect ratios of the geometry are quite large, which implies that there is enough time for the bubbles and the phase fraction to develop along the vertical pipe direction. Pseudo-steady-state can also be reached due to small gas phase fraction and low gas holdup. In test case B.4, non-regular internal pipes are placed in the computational domain and the aspect ratio is relatively small. Meanwhile, it was found in the experiments that the flow field in the pipe is transient due to the existence

of the non-regular internal pipes. These test cases can be distinguished by different features. In our preliminary investigations as mentioned previously, we found that the non-drag forces are crucial to obtain reasonable radial phase fraction distribution, especially for the pseudo-steady-state test cases (e.g., case B.1 to B.3). Therefore, in the following, we will turn our attention to the non-drag forces.

Test case	Exp. data	Features	Pseudo-steady-state
B.1	Phase frac. distri. Upward gas vel.	Wall peak	Yes
B.2	Phase frac. distri.	Double peak	Yes
B.3	Phase frac. distri.	Wall peak Central peak Double peak	Yes
B.4	Global gas holdup	Transient	No

Table 6: Available experimental data and features of test case B.1 to B.4.

Fig. 9 shows the comparison of the upward gas velocity and phase fraction predicted by the $k - \varepsilon$ model with experimental data. It can be seen that the bubble upward velocity is highly dependent on the drag model, which is consistent with the theory and our findings in previous section. The upward gas velocity predicted by the S-N drag model was over-estimated, whereas those predicted by the Grace and I-Z drag model agree well with experimental data. Meanwhile, the wall peak of the gas phase fraction predicted by the Grace and I-Z drag model agree well with the experimental data, whereas the wall peaks predicted by the S-N drag models was sharp. Fig. 10 shows the comparison of the upward gas velocity and phase fraction predicted by the different turbulence models. It can be seen that the predictions of the phase fraction and the upward gas velocity by the $k - \omega$ model were almost identical with those predicted by the $k - \varepsilon$ model. The effect of the addition of the Sato BIT model can be neglected. Both of them predicted the wall peak of the phase fraction distribution with slightly under-estimation. The addition of the Lahey BIT model did not improve the results. On the other hand, it should be noted that all the predicted phase fraction near the wall decrease sharply to a small value, which is not observed in the

experiments. This under-estimation comes from multiple reasons and can be improved by adjusting the wall lubrication model coefficients or including a non-uniform bubble diameter distribution, which will be reported for the following test cases.

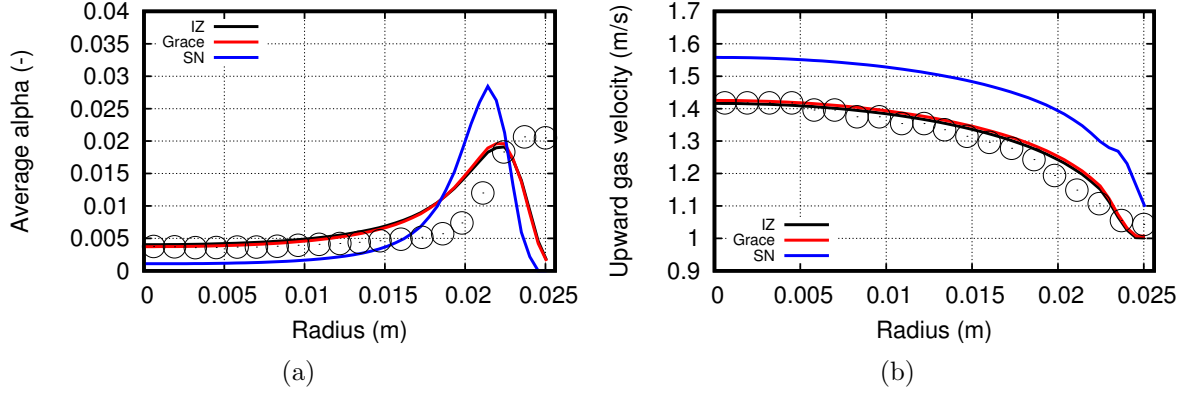


Figure 9: Comparison of the upward gas velocity (lines) and phase fraction (lines) predicted by the $k - \varepsilon$ model and different drag models with experimental data (circles) for test case B.1. Sample location: height of 3.03 m above the inlet.

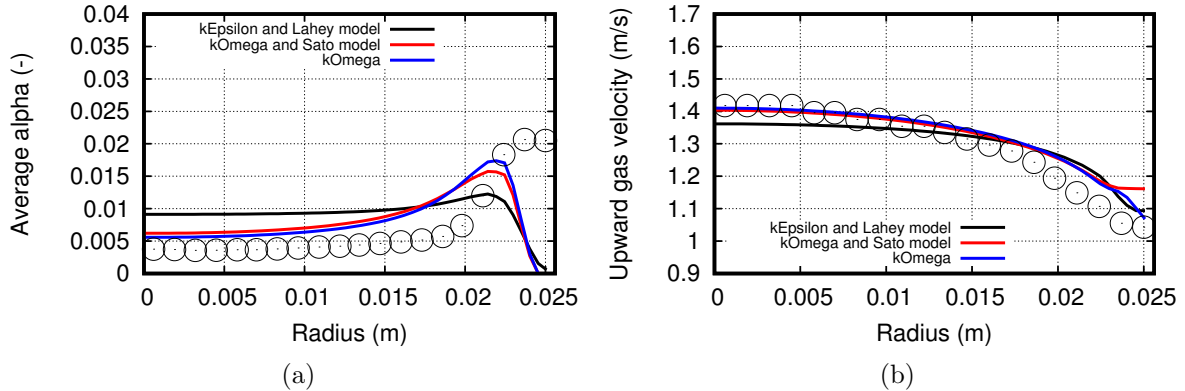


Figure 10: Comparison of the upward gas velocity (lines) and phase fraction (lines) predicted by the Grace model and different turbulence models with experimental data (circles) for test case B.1. Sample location: height of 3.03 m above the inlet.

Fig. 11 shows the radial profiles of the phase fraction predicted by different lift coefficients and bubble diameters for test case B.2. The difference between test case B.1 and B.2 is that a double peak was observed in the latter one due to the existence of bubbles with different diameters. In the mono-disperse plot, the phase fraction of the small bubbles ($d < 5.6$ mm)

was reported. All these small bubbles tend to move towards the wall and the wall peak was observed. Such wall peak was successfully predicted by the lift coefficient calculated by the lift model developed by Tomiyama et al. [35]. Meanwhile, the predicted phase fraction also shows a wall peak in the constant lift model when $C_l > 0$. However, the predict phase fraction shows a center peak when $C_l < 0$. All the results are consistent with the lift theory that the lift force exerted on bubbles can switch sign depending the bubble diameter. The lift coefficient calculated by the Tomiyama lift model is calculated from the bubble diameter, which can automatically change its sign. On the other hand, the results predicted by the constant lift model will be erroneous if a positive C_l was given to large bubbles or a negative C_l was given to small bubbles.

In the poly-disperse plot, a double peak of the phase fraction was observed in the experiments since the phase fraction presents not only for the small bubbles but also for the large bubbles. The large bubbles and small bubbles tend to accumulate at the center and the wall, respectively. Unfortunately, none of the predicted results are satisfactory no matter what bubble diameter was given. This is a notable drawback of the E-E method since only one bubble diameter can be given for the poly-disperse simulations. Therefore, it cannot be used to predict the poly-dispersity. The only solution is to combine the E-E method with the population balance model, in which a non-uniform bubble diameter distribution can be calculated using the population balance equation [72, 73], or to employ a meso-scopic mathematical model (e.g., the generic population balance equation [74, 75]). However, although the E-E method cannot predict the double peak, it can be seen that the predicted phase fraction near the wall is very sensitive to the bubble diameter. The smaller the bubble diameter is, the higher the value phase fraction near the wall will be. This can be explained by the fact that different lift coefficients were predicted when different bubble diameters were used.

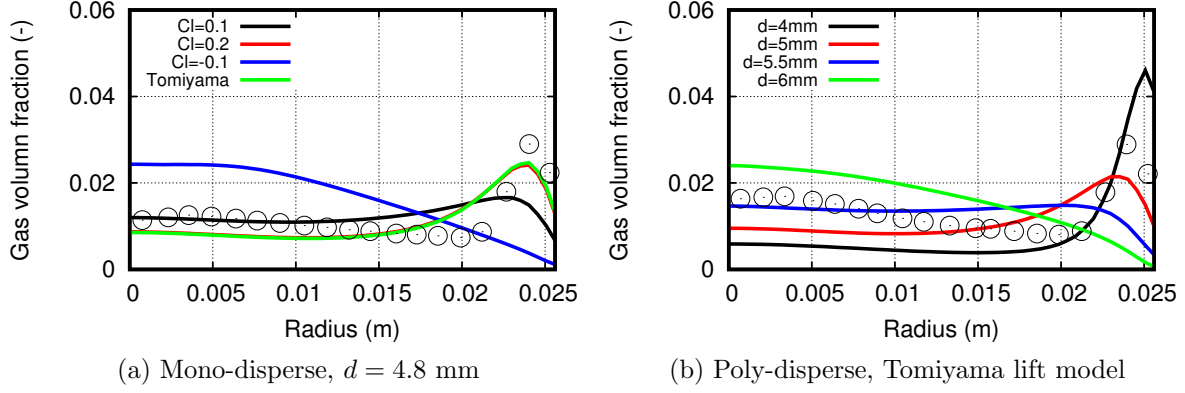


Figure 11: Predicted profiles of the phase fraction (lines) compared with experimental data (circles) for case B.2. $U_g = 0.0151$ m/s. $U_l = 0.534$ m/s. Location: $L/D = 59$. Mono-disperse: exp. data for small bubbles. Poly-disperse: exp. data for small and large bubbles.

Fig. 12 shows the radial profiles of the phase fraction predicted by different wall lubrication coefficients for test case B.3. The wall lubrication model developed by Antal et al. [33] and Hosokawa et al. [76] was investigated. It can be seen that the predicted phase fraction in the vicinity of the wall is highly dependent on the coefficients when the bubble diameter equals 4 mm. Specifically, the wall lubrication force becomes larger when larger C_{wall} was used it pushes the bubbles away from the wall. Decent agreement between the predicted phase fraction with the experimental data can be obtained by adjusting the coefficient. On the other hand, when the bubble diameter is given by 6 mm, the effect of the wall lubrication model on the phase fraction is negligible since the wall lubrication model only acts on the bubbles near the wall region. In such cases a center peak is observed.

Test case B.4 is a upward bubbly pipe flow with relatively small aspect ratio. Only the gas holdup was reported in the literature. The gas holdup predicted by different combinations of the momentum exchange force closure are reported in Table 7. It can be seen that the gas holdup is very sensitive to the drag model. Because the gas velocity predicted by the S-N drag model is higher than those predicted using other drag models, the global gas holdup predicted by the S-N drag model is under-estimated. Moreover, the inclusion of non-drag forces improves the results, which is consistent with previous findings, especially for test case

A.1, B.1 to B.3. Meanwhile, the effect of the BIT model seems to be negligible.

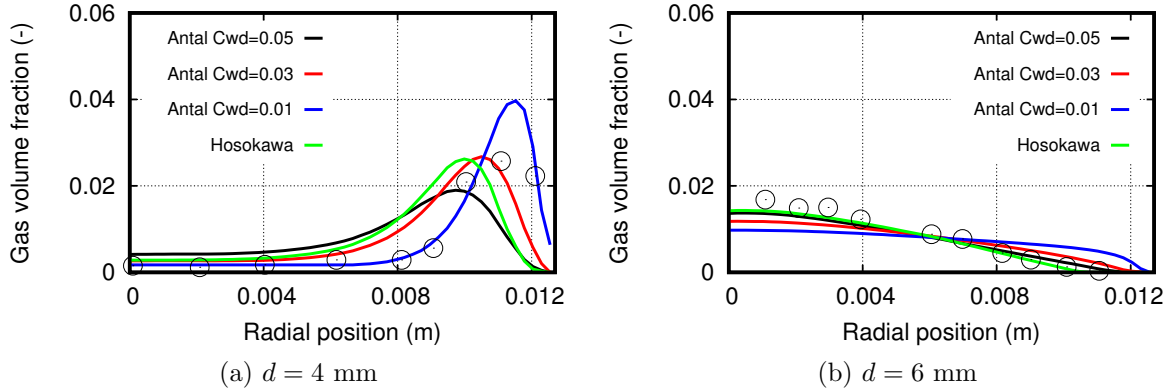


Figure 12: Predicted profiles of the phase fraction (lines) compared with experimental data (circles) by different wall lubrication model for case B.3.

	Drag	Drag & Dis.	Drag & Dis. & Lift	Drag & Dis. & Lift & Wall	Exp.
I-Z, no BIT	0.0061	0.0203	0.024	0.0236	0.0287
I-Z, BIT	0.0073	0.0217	0.0224	0.0225	0.0287
Grace, no BIT	-	-	-	0.0224	0.0287
S-N, no BIT	-	-	-	0.0153	0.0287

Table 7: Predicted gas holdup compared with experimental data for case B.4.

4.3. Test case C.1 - C.2

Test case C.1 and C.2 are common in metallurgical industry. The available experimental data and features are listed in Table 8. In test case C.1, the gas phase is injected into the mold by a submerged entrance nozzle (SEN). Large bubbles are lifted toward the meniscus due to the buoyancy force acting on them and removed from the mold, which smaller bubbles are carried deep into the mold. These small bubbles are trapped in the steel and cause pin hold defects. In the field of numerical simulation, this is also called phase segregation which is very difficult to address. In test case C.2, the gas phase was injected to remove the nonmetallic inclusions in metallurgical reactor. This test case is important because it is the only one for which the turbulent kinetic energy was reported in the experiments.

Test case	Exp. data	Features	Pseudo-steady-state
C.1	Axial liquid vel. Radial liquid vel.	Non-regular flow	Yes
C.2	Axial liquid vel. Turbulent kinetic energy	Central bubble plume	Yes

Table 8: Available experimental data and features of test case C.1 to C.2.

Fig. 13 shows the axial and radial liquid velocities predicted by different drag models and different bubble diameters. It can be seen that all these drag models can predict accurate axial liquid velocity compared with experimental data. Meanwhile, it can be found that the predicted axial liquid velocity is not sensitive to the bubble diameters. On the other hand, none of the models can predict satisfactory radial liquid velocity. The predicted radial liquid velocities at the right tail of the plot were smaller than 0, which implies the liquid is moving toward the bottom of the mold and a large vortex at the right bottom of the mold is formed. Using a smaller bubble diameter improves the predictions due to the effect of the small bubbles upward movement on the liquid velocity. Such inconsistency may come from the mono-disperse assumption of the E-E method and can be handled by using a poly-disperse model. Fig. 14 shows the average phase fraction predicted when different bubble diameters were employed. It can be seen that the smaller the bubbles are, the farther they move. It is consistent with the theory that the drag force exerted on the smaller bubbles is larger, and they are convected farther by the liquid flow. Meanwhile, those small bubbles' upward movement has an important effect on the liquid velocity. At last, it should be noted here that the addition of non-drag forces had no clear significant effect on the results, therefore the results are not shown here for brevity.

Fig. 15 shows the predicted axial liquid velocity and turbulent kinetic energy with and without the BIT models. The S-N drag model and turbulence dispersion model was used. It can be seen that the axial liquid velocity predicted without the BIT model agree well with the experimental data. However, the predictions by the BIT model were under-estimated. It can be explained by the over-prediction of the turbulent viscosity which introduces a

damping effect. On the other hand, all these models failed to predict the turbulent kinetic energy. Such unsatisfactory predictions can be also found in the work of Sheng et al. [68], in which they developed a modified $k - \varepsilon$ to handle such problem. However, this model is only suggested to the gas-liquid two-phase plumes for ladle metallurgy processes. Meanwhile, it should be noted that the effect of the lift and wall lubrication forces are negligible, since the investigated area is far away from the wall region.

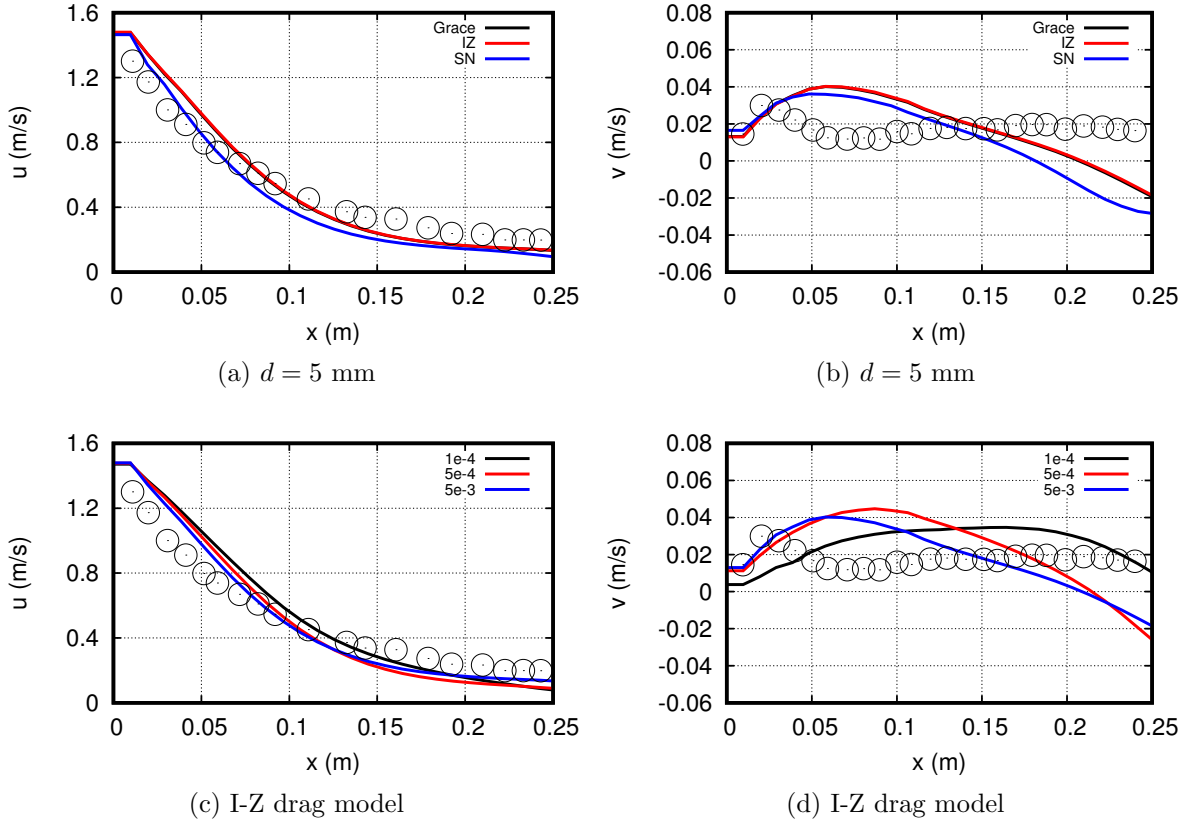


Figure 13: Comparison of the axial and radial liquid velocity predicted by different drag models and different diameters with experimental data (points).

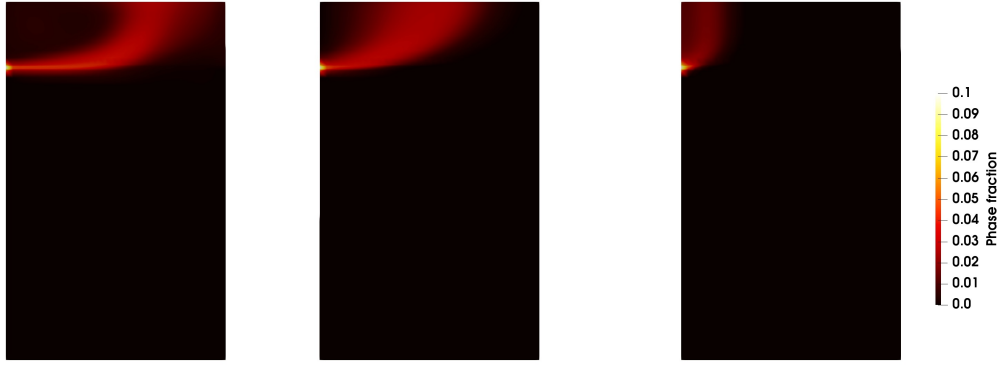


Figure 14: Predicted average phase fraction inside the mold for test case C.1 when different bubble diameters were used. Left: $d = 0.1$ mm, middle: $d = 0.5$ mm, right: $d = 5$ mm.

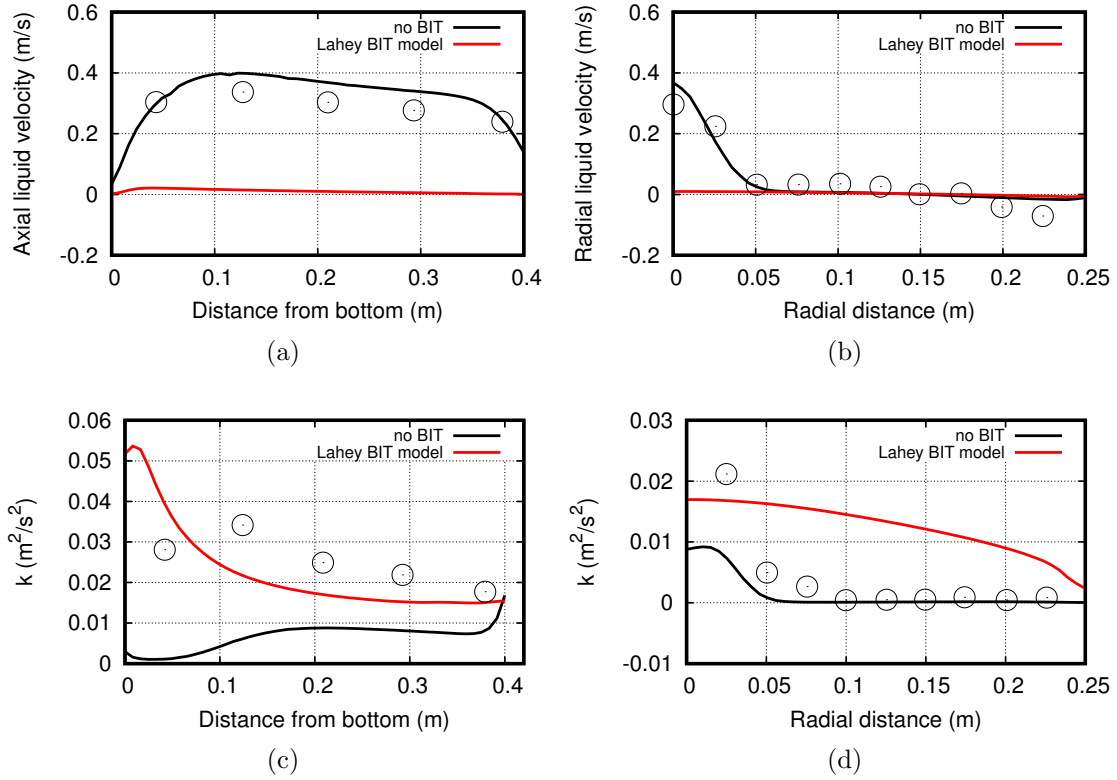


Figure 15: Comparison of the predicted axial liquid velocity and turbulent kinetic energy (lines) and experimental data (points) with and without BIT models. Monitoring location: along the center line of the bubble plume.

5. Conclusions

In this work, we performed numerical study of the Eulerian-Eulerian method by nine bubbly flow test cases. Simulation results were compared against experimental data. Here, we list some universal principles that are useful when employing the E-E method to simulate bubbly flows.

- It is recommended to include drag force and turbulence dispersion force in the E-E method to simulate bubbly flows. The drag force, as the most important momentum exchange term, plays the most important role on the prediction of the local phase fraction, global holdup and gas/liquid velocities. The turbulence dispersion force should be included as well to address the pseudo-turbulence effect, otherwise the gas phase tends to accumulate locally.
- The lift force and wall lubrication force are crucial to predict accurate radial phase fraction distribution in the pipe flows with large aspect ratio (e.g., test case B.1 - B.3) where the gas phase has enough time to develop a wall peak or double peak distribution. In other cases, these forces can be safely neglected. Meanwhile, it should be noted that these non-drag forces are rather sensitive to model parameters.
- When the gas phase fraction is high (e.g., larger than 10%), the bubble swarm model needs to be included to account for the reduction in drag, otherwise the phase fraction and gas holdup will be over-estimated (e.g., test case A.2).
- In some cases studied in this work, the effect of the BIT model is negligible (e.g., test case A and C.1). In other cases, the addition of the BIT model introduces even worse results (e.g., test case B and C.2). However, it was shown in many other works that the addition of the BIT improves the predictions. Meanwhile, prediction of the turbulence variables was proven as a quite difficult task because of the coupled effects of shear, wake phenomena, mesh resolution and turbulence model as well as the BIT. Further work is clearly needed to improve the accuracy of the multi-phase turbulence model.

It is the authors' experience that the results investigated in this work is highly sensitive to the model setting, and this is not discovered until one tries to investigate the model. It is therefore the author's wish that these bubbly flow test cases can be useful to those working on similar areas. All the source codes are therefore available as Mendeley Data for anyone to download.

Contributions

Yulong Li: wrote the paper; post-processed the data; performed the analysis. Dongyue Li: conceived the analysis; corrected the paper; prepared the OpenFOAM test cases.

Acknowledgement

One of the author (Dongyue Li) wants to acknowledge the CFD-China community for the fruitful discussions of gas-liquid flows.

References

References

- [1] H.A. Jakobsen, H. Lindborg, and C.A. Dorao. Modeling of bubble column reactors: progress and limitations. *Industrial & engineering chemistry research*, 44:5107–5151, 2005.
- [2] V.V. Buwa, D.S. Deo, and V.V. Ranade. Eulerian–Lagrangian simulations of unsteady gas–liquid flows in bubble columns. *International Journal of Multiphase Flow*, 32:864–885, 2006.
- [3] G. Li, X. Yang, and G. Dai. CFD simulation of effects of the configuration of gas distributors on gas–liquid flow and mixing in a bubble column. *Chemical Engineering Science*, 64:5104–5116, 2009.

- [4] G. Li, Q. Cai, G. Dai, and X. Yang. Numerical simulations of fluid dynamics and mixing in a large shallow bubble column: effects of the sparging pipe allocations for multiple-pipe gas distributors. *International Journal of Engineering Systems Modelling and Simulation*, 1:165–175, 2009.
- [5] M. Banaei, J. Jegers, M. Van Sint Annaland, J.A.M. Kuipers, and N.G. Deen. Tracking of particles using TFM in gas-solid fluidized beds. *Advanced Powder Technology*, 29: 2538–2547, 2018.
- [6] M. Banaei, N.G. Deen, M. Van Sint Annaland, and J.A.M. Kuipers. Particle mixing rates using the two-fluid model. *Particuology*, 36:13–26, 2018.
- [7] V.H. Bhusare, D.V. Kalaga, M.K. Dhiman, J.B. Joshi, and S. Roy. Mixing in a co-current upflow bubble column reactors with and without internals. *The Canadian Journal of Chemical Engineering*, 96:1957–1971, 2018.
- [8] W. Shi, X. Yang, M. Sommerfeld, J. Yang, X. Cai, G. Li, and Y. Zong. Modelling of mass transfer for gas-liquid two-phase flow in bubble column reactor with a bubble breakage model considering bubble-induced turbulence. *Chemical Engineering Journal*, 371:470–485, 2019.
- [9] J.T. Padding, N.G. Deen, E. Peters, and J.A.M. Kuipers. Euler–Lagrange modeling of the hydrodynamics of dense multiphase flows. In *Advances in Chemical Engineering*, volume 46, pages 137–191. Elsevier, 2015.
- [10] A. Quiyoom, V.V. Buwa, and S.K. Ajmani. Euler-Lagrange simulations of gas-liquid flow in a basic oxygen furnace and experimental verification. In *Fluid Mechanics and Fluid Power–Contemporary Research*, pages 1151–1161. Springer, 2017.
- [11] A. Battistella, S. Aelen, I. Roghair, and M. Van Sint Annaland. Euler–Lagrange modeling of bubbles formation in supersaturated water. *ChemEngineering*, 2:39, 2018.

- [12] N.G Deen and J.A.M. Kuipers. Direct numerical simulation (DNS) of mass, momentum and heat transfer in dense fluid-particle systems. *Current Opinion in Chemical Engineering*, 5:84–89, 2014.
- [13] S. Das, N.G. Deen, and J.A.M. Kuipers. A DNS study of flow and heat transfer through slender fixed-bed reactors randomly packed with spherical particles. *Chemical Engineering Science*, 160:1–19, 2017.
- [14] S.S. Rabha and V.V. Buwa. Volume-of-fluid (VOF) simulations of rise of single/multiple bubbles in sheared liquids. *Chemical Engineering Science*, 65:527–537, 2010.
- [15] D. Goel and V.V. Buwa. Numerical simulations of bubble formation and rise in microchannels. *Industrial & Engineering Chemistry Research*, 48:8109–8120, 2008.
- [16] R. Rzehak, T. Ziegenhein, S. Kriebitzsch, E. Krepper, and D. Lucas. Unified modeling of bubbly flows in pipes, bubble columns, and airlift columns. *Chemical Engineering Science*, 157:147–158, 2017.
- [17] T. Ziegenhein and D. Lucas. The critical bubble diameter of the lift force in technical and environmental, buoyancy-driven bubbly flows. *International Journal of Multiphase Flow*, 116:26–38, 2019.
- [18] H. Hessenkemper, T. Ziegenhein, and D. Lucas. Contamination effects on the lift force of ellipsoidal air bubbles rising in saline water solutions. *Chemical Engineering Journal*, 2019.
- [19] A. Buffo, M. Vanni, P. Renze, and D.L. Marchisio. Empirical drag closure for polydisperse gas–liquid systems in bubbly flow regime: Bubble swarm and micro-scale turbulence. *Chemical Engineering Research and Design*, 113:284–303, 2016.
- [20] I. Roghair, M. Van Sint Annaland, and J.A.M. Kuipers. Drag force and clustering in bubble swarms. *AIChE Journal*, 59(5):1791–1800, 2013.

- [21] I. Roghair, M.W. Baltussen, M. Van Sint Annaland, and J.A.M. Kuipers. Direct numerical simulations of the drag force of bi-disperse bubble swarms. *Chemical Engineering Science*, 95:48–53, 2013.
- [22] Y. Sato and K. Sekoguchi. Liquid velocity distribution in two-phase bubble flow. *International Journal of Multiphase Flow*, 2:79–95, 1975.
- [23] Y. Liao, T. Ma, E. Krepper, D. Lucas, and J. Fröhlich. Application of a novel model for bubble-induced turbulence to bubbly flows in containers and vertical pipes. *Chemical Engineering Science*, 2019.
- [24] T. Ma, C. Santarelli, T. Ziegenhein, D. Lucas, and J. Fröhlich. Direct numerical simulation–based Reynolds-averaged closure for bubble-induced turbulence. *Physical Review Fluids*, 2:034301, 2017.
- [25] R. Rzehak and E. Krepper. Bubble-induced turbulence: Comparison of CFD models. *Nuclear Engineering and Design*, 258:57–65, 2013.
- [26] A. Vaidheeswaran and T. Hibiki. Bubble-induced turbulence modeling for vertical bubbly flows. *International Journal of Heat and Mass Transfer*, 115:741–752, 2017.
- [27] A. Vaidheeswaran and M. Lopez De Bertodano. Stability and convergence of computational Eulerian two-fluid model for a bubble plume. *Chemical Engineering Science*, 160:210–226, 2017.
- [28] N. Panicker, A. Passalacqua, and R.O. Fox. On the hyperbolicity of the two-fluid model for gas–liquid bubbly flows. *Applied Mathematical Modelling*, 57:432–447, 2018.
- [29] C.M. Rhie and W.L. Chow. Numerical study of the turbulent flow past an airfoil with trailing edge separation. *AIAA journal*, 21:1525–1532, 1983.
- [30] S. Zhang, X. Zhao, and S. Bayyuk. Generalized formulations for the Rhie-Chow interpolation. *Journal of Computational Physics*, 258:880–914, 2014.

- [31] D.A. Drew. Mathematical modeling of two-phase flow. *Annual Review of Fluid Mechanics*, 15:261–291, 1982.
- [32] A. Tomiyama, H. Tamai, I. Zun, and S. Hosokawa. Transverse migration of single bubbles in simple shear flows. *Chemical Engineering Science*, 57:1849–1858, 2002.
- [33] S.P. Antal, R.T. Lahey, and J.E. Flaherty. Analysis of phase distribution in fully developed laminar bubbly two-phase flow. *International Journal of Multiphase Flow*, 17:635–652, 1991.
- [34] M. Lopez De Bertodano. *Turbulent bubbly two-phase flow in a triangular duct*. PhD thesis, Rensselaer Polytechnic Institute, 1992.
- [35] A. Tomiyama, A. Sou, I. Zun, N. Kanami, and T. Sakaguchi. Effects of Eötvös number and dimensionless liquid volumetric flux on lateral motion of a bubble in a laminar duct flow. *Advances in multiphase flow*, 1995:3–15, 1995.
- [36] M. Ishii and T. Hibiki. *Thermo-fluid dynamics of two-phase flow*. Springer Science & Business Media, 2010.
- [37] M. Lopez De Bertodano, W. Fullmer, A. Clausse, and V. Ransom. *Two-Fluid Model Stability, Simulation and Chaos*. Springer, 2016.
- [38] E. Krepper, D. Lucas, and H. Prasser. On the modelling of bubbly flow in vertical pipes. *Nuclear engineering and design*, 235:597–611, 2005.
- [39] G. Besagni, F. Inzoli, T. Ziegenhein, and D. Lucas. Computational Fluid-Dynamic modeling of the pseudo-homogeneous flow regime in large-scale bubble columns. *Chemical Engineering Science*, 160:144–160, 2017.
- [40] K. Bech. Dynamic simulation of a 2D bubble column. *Chemical engineering science*, 60:5294–5304, 2005.

- [41] S.L. Sharma, T. Hibiki, M. Ishii, J.P. Schlegel, J.R. Buchanan, K.J. Hogan, and P.W. Guilbert. An interfacial shear term evaluation study for adiabatic dispersed air–water two-phase flow with the two-fluid model using CFD. *Nuclear Engineering and Design*, 312:389–398, 2017.
- [42] V.H. Bhusare, M.K. Dhiman, D.V. Kalaga, S. Roy, and J.B. Joshi. CFD simulations of a bubble column with and without internals by using OpenFOAM. *Chemical Engineering Journal*, 317:157–174, 2017.
- [43] R.T. Lahey. The simulation of multidimensional multiphase flows. *Nuclear Engineering and Design*, 235:1043–1060, 2005.
- [44] R.T. Lahey and D.A. Drew. The analysis of two-phase flow and heat transfer using a multidimensional, four field, two-fluid model. *Nuclear Engineering and Design*, 204:29–44, 2001.
- [45] P.J. Oliveira and R.I. Issa. On the numerical treatment of interphase forces in two-phase flow. *ASME Publications Fed*, 185:131–131, 1994.
- [46] A. Passalacqua and R.O. Fox. Implementation of an iterative solution procedure for multi-fluid gas–particle flow models on unstructured grids. *Powder Technology*, 213:174–187, 2011.
- [47] H. Weller. OpenFOAM-2.3.x. <https://github.com/OpenFOAM/OpenFOAM-2.3.x>, 2015.
- [48] D.R. Shaver and M.Z. Podowski. Modeling of interfacial forces for bubbly flows in subcooled boiling conditions. *Trans. Am. Nucl. Soc.(Proc. ANS Winter Mtg.)*, 113:1368, 2015.
- [49] H. Weller. OpenFOAM-6. <https://github.com/OpenFOAM/OpenFOAM-6>, 2018.
- [50] D. Li and H. Christian. Simulation of bubbly flows with special numerical treatments

- of the semi-conservative and fully conservative two-fluid model. *Chemical Engineering Science*, 174:25–39, 2017.
- [51] R.I. Issa, A.D. Gosman, and A.P. Watkins. The computation of compressible and incompressible recirculating flows by a non-iterative implicit scheme. *Journal of Computational Physics*, 62:66–82, 1986.
- [52] M. Ishii. Thermo-fluid dynamic theory of two-phase flow. *NASA STI/Recon Technical Report A*, 75:29657, 1975.
- [53] D.B. Spalding. Numerical computation of multi-phase fluid flow and heat transfer. *Recent Advance in Numerical Methods Fluids*, 1:139–167, 1980.
- [54] M.E. Díaz, A. Iranzo, D. Cuadra, R. Barbero, F.J. Montes, and M.A. Galán. Numerical simulation of the gas–liquid flow in a laboratory scale bubble column: influence of bubble size distribution and non-drag forces. *Chemical Engineering Journal*, 139:363–379, 2008.
- [55] A. Sokolichin, G. Eigenberger, A. Lapin, and A. Lübert. Dynamic numerical simulation of gas-liquid two-phase flows Euler/Euler versus Euler/Lagrange. *Chemical Engineering Science*, 52:611–626, 1997.
- [56] D. McClure, H. Norris, J. Kavanagh, D. Fletcher, and G. Barton. Validation of a computationally efficient computational fluid dynamics (cfd) model for industrial bubble column bioreactors. *Industrial & Engineering Chemistry Research*, 53:14526–14543, 2014.
- [57] R. Bel F’dhila. *Analyse expérimentale et modélisation d’un écoulement vertical à bulles dans un élargissement brusque*. PhD thesis, Toulouse, INPT, 1991.
- [58] A Behzadi, R.I. Issa, and H. Rusche. Modelling of dispersed bubble and droplet flow at high phase fractions. *Chemical Engineering Science*, 59:759–770, 2004.

- [59] P.J. Oliveira and R.I. Issa. Numerical aspects of an algorithm for the Eulerian simulation of two-phase flows. *International Journal for Numerical Methods in Fluids*, 43:1177–1198, 2003.
- [60] D. Cokljat, M. Slack, S.A. Vasquez, A. Bakker, and G. Montante. Reynolds-stress model for eulerian multiphase. *Progress in Computational Fluid Dynamics, An International Journal*, 6:168–178, 2006.
- [61] M. Ullrich. *Second-moment closure modeling of turbulent bubbly flows within the two-fluid model framework*. PhD thesis, Technische Universität, 2017.
- [62] D. Lucas, E. Krepper, and H.M. Prasser. Development of co-current air–water flow in a vertical pipe. *International Journal of Multiphase Flow*, 31:1304–1328, 2005.
- [63] A. Tomiyama, I. Kataoka, I. Zun, and T. Sakaguchi. Drag coefficients of single bubbles under normal and micro gravity conditions. *JSME International Journal Series B Fluids and Thermal Engineering*, 41:472–479, 1998.
- [64] M. Banowski, U. Hampel, E. Krepper, M. Beyer, and D. Lucas. Experimental investigation of two-phase pipe flow with ultrafast X-ray tomography and comparison with state-of-the-art CFD simulations. *Nuclear Engineering and Design*, 336:90–104, 2018.
- [65] I. Žun. The mechanism of bubble non-homogeneous distribution in two-phase shear flow. *Nuclear Engineering and Design*, 118:155–162, 1990.
- [66] G. Besagni, G. Guédon, and F. Inzoli. Annular gap bubble column: experimental investigation and computational fluid dynamics modeling. *Journal of Fluids Engineering*, 138:011302, 2016.
- [67] M. Iguchi and N. Kasai. Water model study of horizontal molten steel–air two-phase jet in a continuous casting mold. *Metallurgical and Materials Transactions B*, 31:453–460, 2000.

- [68] Y.Y. Sheng and G.A. Irons. Measurement and modeling of turbulence in the gas/liquid two-phase zone during gas injection. *Metallurgical Transactions B*, 24:695–705, 1993.
- [69] A. Tomiyama, I. Kataoka, T. Fukuda, and T. Sakaguchi. Drag coefficients of bubbles: 2nd report, drag coefficient for a swarm of bubbles and its applicability to transient flow. *JSME Journal of Fluid Engineering*, 61:2810–2817, 1995.
- [70] X. Liang, H. Pan, Y. Su, and Z. Luo. CFD-PBM approach with modified drag model for the gas–liquid flow in a bubble column. *Chemical Engineering Research and Design*, 112:88–102, 2016.
- [71] H. Rusche. *Computational fluid dynamics of dispersed two-phase flows at high phase fractions*. PhD thesis, Imperial College London, 2003.
- [72] C. Peña-Monferrer, A. Passalacqua, S. Chiva, and J.L. Muñoz-Cobo. CFD modelling and validation of upward bubbly flow in an adiabatic vertical pipe using the quadrature method of moments. *Nuclear Engineering and Design*, 301:320–332, 2016.
- [73] D. Lucas, T. Frank, C. Lifante, P. Zwart, and A. Burns. Extension of the inhomogeneous MUSIG model for bubble condensation. *Nuclear Engineering and Design*, 241:4359–4367, 2011.
- [74] D. Li, D.L. Marchisio, C. Hasse, and D. Lucas. twoWayGPBEFoam and oneWayGPBEFoam: open-source Eulerian-QBMM solvers for multiphase flows. *Computer Physics Communications*, Submitted.
- [75] D. Li, D.L. Marchisio, C. Hasse, and D. Lucas. Comparison of Eulerian-QBMM and classical Eulerian-Eulerian method for the simulation of poly-disperse bubbly flows. *AIChE Journal*, Submitted.
- [76] S. Hosokawa, A. Tomiyama, S. Misaki, and T. Hamada. Lateral migration of single bub-

bles due to the presence of wall. In *ASME 2002 Joint US-European Fluids Engineering Division Conference*, pages 855–860. American Society of Mechanical Engineers, 2002.